

# **The effect of chemical substitution on the local structure of garnet-type oxides that have nuclear waste sequestration applications**

A Thesis submitted to the  
College of Graduate and Postdoctoral Studies  
In Partial Fulfillment of the Requirements  
For the Degree of Master of Science  
In the Department of Chemistry  
University of Saskatchewan  
Saskatoon, Canada

By  
**Rahin Sifat**

© Copyright Rahin Sifat, August 2018. All rights reserved.

## Permission to Use

In presenting this thesis in partial fulfillment of the requirements for a degree of Master from the University of Saskatchewan, I agree that the Libraries of this University may make it freely available for inspection. I further agree that permission for copying of this thesis in any manner, in whole or in part, for scholarly purposes may be granted by the professor or professors who supervised my thesis work or, in their absence, by the Head of the Department or the Dean of the College in which my thesis work was done. It is understood that any copying or publication or use of this thesis or parts thereof for financial gain shall not be allowed without my written permission. It is also understood that due recognition shall be given to me and to the University of Saskatchewan in any scholarly use which may be made of any material in my thesis.

Requests for permission to copy or to make other uses of materials in this thesis in whole or part should be addressed to:

Head of the Department of Chemistry  
University of Saskatchewan  
Saskatoon, Saskatchewan S7N 5C9  
Canada

OR

Dean  
College of Graduate and Postdoctoral Studies  
University of Saskatchewan  
116 Thorvaldson Building, 110 Science Place  
Saskatoon, Saskatchewan S7N 5C9  
Canada

## Abstract

The garnet-type structure has been investigated widely for numerous applications (i.e. laser, battery, diode etc.). The structure shows high chemical flexibility and compositional diversity. Material properties can be tuned and influenced by chemical substitution of garnet type materials. Garnet has recently been investigated as a potential host matrix for the immobilization of actinide elements found in high level nuclear waste. The general formula unit of garnet is  $X_3A_2B_3O_{12}$ . The structure has three different polyhedral sites with different sizes and coordination numbers: 8 coordinate dodecahedral site (X-site); 6 coordinate octahedral site (A-site); and 4 coordinate tetrahedral site (B-site). To understand the effect of chemical substitution in cation site disorder, four different series of garnet-type materials ( $Y_3Al_xGa_{5-x}O_{12}$ ,  $Y_3Al_xFe_{5-x}O_{12}$ ,  $Y_3Ga_xFe_{5-x}O_{12}$ , and  $Y_3Al_xGa_yFe_{5-x-y}O_{12}$ ) were initially synthesized under the same conditions. The local structures of the A- and B- sites were investigated to understand the site occupancies. Factors that affect the site preference of Al, Ga, and Fe were studied using powder XRD and X-ray absorption near edge spectroscopy (XANES).

For further study, a series of garnet materials ( $Y_{3-z}Ce_zAlFe_4O_{12}$ ) was investigated in to understand the factors affecting the oxidation state of Ce, which can be used as a simulator element for actinides. Powder XRD and XANES have been used to study the change in oxidation state of Ce in  $Y_{3-z}Ce_zAlFe_4O_{12}$  ( $0.05 \leq z \leq 0.20$ ) materials. The Ce  $L_3$ -edge spectra confirmed that Ce has a mixture of oxidation state (3+ and 4+) in the system. The largest concentration of  $Ce^{4+}$  was observed when the materials were post-annealed at 800 °C following synthesis of the materials at 1400 °C. The observation of this variation in Ce oxidation state is a result of the temperature dependant  $Ce^{3+}/Ce^{4+}$  redox couple with  $Ce^{4+}$  being favoured at lower temperatures. Examination of the Fe K-edge XANES spectra indicated that only  $Fe^{3+}$  was present within the materials and

that the average Fe coordination number increased with increasing concentration of  $\text{Ce}^{4+}$  to charge balance the system. This study suggests that this system can be described as an oxygen-stuffed garnet-type structure with the formula being  $\text{Y}_{3-z}\text{Ce}_z\text{AlFe}_4\text{O}_{12+\delta}$ .

## Acknowledgements

First and foremost, I am greatly indebted to my advisor, Dr. Andrew P. Grosvenor, who has provided direction and advice over the course of my research. I consider myself very fortunate to receive his valuable guidance and feedback for my manuscripts and thesis. Dr. Andrew P. Grosvenor has provided direction and advice over the course of the research presented and provided many helpful and beneficial revisions to the written material. Besides my advisor, I would like to thank the advisory committee member, Dr. Robert W. J. Scott, for his insightful comments and support.

Except where noted otherwise, I carried out the synthesis, characterization, interpretation, and writing presented in this thesis. I would like to acknowledge the beamline scientists for their help ensuring the synchrotron experiments were a success. I am thankful to Dr. Yongfeng Hu, Ms. Aimee MacLennan, and Dr. Lucia Zuin their support in carrying out experiments at the CLS and Dr. George Sterbinsky, Dr. Tianpin Wu, Dr Zou Finfrock, and Dr. Mathew Ward for their support in carrying out experiments at the APS. Additionally, I would like to thank the current and past members of the Grosvenor group for their help and support during my M.Sc. I would especially like to thank Dr. Jeremy Beam, Dr. Xiaoxuan Guo, Dr. M. Ruwaid Rafiuddin, and Ms. Sarah McCaugherty for their help collecting the XANES spectra presented in Chapter 2 and Chapter 3.

# Contents

<b>1</b>	<b>Introduction .....</b>	<b>1</b>
1.1	Introduction: .....	1
1.2	Crystal structure of garnet: .....	2
1.3	Nuclear waste generation and management: .....	3
1.3.1	Nuclear wasteforms: .....	6
1.4	Experimental techniques: .....	9
1.4.1	Powder X-ray diffraction (XRD): .....	9
1.4.2	X-ray absorption spectroscopy (XAS): .....	10
1.4.3	X-ray Absorption Near-edge Spectroscopy (XANES): .....	11
1.4.4	Experimental Setups: .....	15
1.5	Thesis overview: .....	19
<b>2</b>	<b>Examination of the site preference in garnet type (<math>X_3A_2B_3O_{12}</math>; <math>X=Y</math>, <math>A/B=Al, Ga, Fe</math>) materials* .....</b>	<b>21</b>
2.1	Introduction: .....	21
2.2	Experimental: .....	22
2.2.1	Synthesis: .....	22
2.3	XANES.....	23
2.3.1	Al $L_{2,3}$ - edge XANES: .....	23
2.3.2	Ga K- and Fe K-edge XANES: .....	23
2.4	Results and discussion: .....	24
2.4.1	Powder XRD: .....	24
2.5	XANES: .....	29
2.5.1	Al $L_{2,3}$ -edge XANES: .....	29
2.5.2	Ga K-edge XANES: .....	34

2.5.3	Fe K-edge XANES: .....	37
2.6	Conclusions: .....	40
<b>3</b>	<b>Investigation of the factors affecting the oxidation state of Ce in the garnet structure* .....</b>	<b>41</b>
3.1	Introduction: .....	41
3.2	Experimental: .....	42
3.2.1	Synthesis and Powder XRD:.....	42
3.2.2	X-ray absorption near-edge spectroscopy (XANES):.....	43
3.3	Results and discussion:.....	44
3.3.1	Powder XRD:.....	44
3.3.2	Ce L <sub>3</sub> -edge XANES spectra:.....	45
3.3.3	Fe K-edge XANES spectra: .....	52
3.4	Conclusions: .....	55
<b>4</b>	<b>Conclusions and Future work .....</b>	<b>56</b>
4.1	Conclusions and significance: .....	56
4.1.1	Effect of studying the A- and B- site preference: .....	56
4.1.2	Effect of studying the factors affecting the oxidation state of Ce: .....	57
4.2	Direction for future work: .....	58
	<b>References.....</b>	<b>61</b>

## List of Tables:

<b>Table 2-1:</b> Change in the lattice constants in the quinary ( $\text{Y}_3\text{Al}_x\text{Ga}_y\text{Fe}_{5-x-y}\text{O}_{12}$ ) system. ....	26
<b>Table 2-2:</b> Rietveld refinement parameters for $\text{Y}_3\text{Al}_x\text{Ga}_{5-x}\text{O}_{12}$ .....	28
<b>Table 3-1:</b> Labels and descriptions of different samples studied- .....	43



## List of Figures:

<b>Figure 1-1:</b> A schematic representation of the garnet structure is shown. Blue, red, and black polyhedra represent the 8-, 6-, and 4-coordinate sites, respectively. Red spheres represent the oxygen atoms. ....	3
<b>Figure 1-2:</b> Schematic diagram of Bragg's law. When X-rays (wavelength, $\lambda$ ) are incident on a lattice plane at an angle $\theta$ , some of the X-rays undergo constructive interference. ....	10
<b>Figure 1-3:</b> A schematic layout of a synchrotron radiation facility is presented. The electrons are accelerated to high energies using a linear accelerator. The electrons travel with a relativistic speed through the booster ring and storage ring maintaining a circular path. The storage ring consists of bending magnets and insertion devices, which are responsible for the generation of the most intense synchrotron radiation. ....	13
<b>Figure 1-4:</b> X-ray absorption spectrum from $\text{Y}_3\text{Fe}_5\text{O}_{12}$ , showing the XANES and EXAFS regions. The XANES spectrum is further divided into pre-edge and main-edge regions. ....	14
<b>Figure 1-5:</b> X-ray transitions commonly observed in the vicinity of metal K-edges include the dipole forbidden $1s \rightarrow (n-1)d$ transitions, and the dipole allowed $1s \rightarrow (n-1)p$ . L-edge includes dipole allowed $2p \rightarrow ns$ and $2p \rightarrow (n-1)d$ transitions. ....	14
<b>Figure 1-6:</b> An incident beam of monochromatic X-ray with intensity $I_0$ passes through a sample of thickness $t$ . The transmission beam has intensity $I_t$ . The absorption coefficient is followed by Beer-Lambert law. ....	16
<b>Figure 1-7:</b> Hard X-ray transmission and fluorescence set-up. The X-ray photon beam from the ionization chamber ( $I_0$ ) is transmitted through the sample and the transmitted beam is measured using an ionization chamber ( $I_t$ ). The released fluorescence photons ( $I_f$ ) are collected using fluorescence detector. ....	17
<b>Figure 1-8:</b> The excited atom leaves a core-hole (i.e., unoccupied state) while the electron in the excited state relaxes to lower energy to fill the core-hole. ....	19
<b>Figure 1-9:</b> The ultra-high vacuum chamber for the VLS-PGM Beamline located at the Canadian Light Source in Saskatoon, SK. Entering via the beam pipe, the X-ray beam travels into the XAS chamber striking the sample (S), and the fluorescence ( $I_F$ ) signal is collected at a detector attached to one of the chamber ports. ....	19

**Figure 2-1:** Normalized powder X-ray diffraction patterns collected from a)  $\text{Y}_3\text{Al}_x\text{Ga}_{5-x}\text{O}_{12}$ , b)  $\text{Y}_3\text{Ga}_x\text{Fe}_{5-x}\text{O}_{12}$ , c)  $\text{Y}_3\text{Al}_x\text{Fe}_{5-x}\text{O}_{12}$ , and d)  $\text{Y}_3\text{Al}_x\text{Ga}_y\text{Fe}_{5-x-y}\text{O}_{12}$  are shown. The XRD patterns collected using a Cu source were converted to show how they would appear if a Co source was used for easy comparison between the four systems investigated. .... 25

**Figure 2-2:** The change in lattice constant from the ternary systems is presented as a function of 'x'. .... 26

**Figure 2-3:** Results of the Rietveld refinement of powder XRD patterns from (a)  $\text{Y}_3\text{AlGa}_4\text{O}_{12}$ , (b)  $\text{Y}_3\text{Al}_2\text{Ga}_3\text{O}_{12}$ , (c)  $\text{Y}_3\text{Al}_3\text{Ga}_2\text{O}_{12}$ , and (d)  $\text{Y}_3\text{Al}_4\text{GaO}_{12}$  are presented. .... 27

**Figure 2-4:** Change in  $\text{Al}^{3+}$  and  $\text{Ga}^{3+}$   $\text{O}_h/\text{T}_d$  site occupancy ratio as a function of 'x'. .... 29

**Figure 2-5:** Normalized Al  $\text{L}_{2,3}$ - edge spectra are presented from a)  $\text{Y}_3\text{Al}_x\text{Ga}_{5-x}\text{O}_{12}$ , b)  $\text{Y}_3\text{Al}_x\text{Fe}_{5-x}\text{O}_{12}$ , and c)  $\text{Y}_3\text{Al}_x\text{Ga}_y\text{Fe}_{5-x-y}\text{O}_{12}$ . Peak A corresponds to Al in the tetrahedral site while peak B corresponds to Al in octahedral site. Arrows indicate the change in intensity of peak A and peak B with increasing Al concentration. .... 30

**Figure 2-6:** Normalized Ga K-edge from a)  $\text{Y}_3\text{Al}_x\text{Ga}_{5-x}\text{O}_{12}$ , b)  $\text{Y}_3\text{Ga}_x\text{Fe}_{5-x}\text{O}_{12}$ , and c)  $\text{Y}_3\text{Al}_x\text{Ga}_y\text{Fe}_{5-x-y}\text{O}_{12}$ . Peak A corresponds to  $\text{Ga}^{3+}$  in occupying the tetrahedral site and peak B corresponds to  $\text{Ga}^{3+}$  occupying the octahedral site. Arrows indicate the change in intensity of peak A and peak B with increasing 'x' (a) and (b) or 'y' (c)..... 35

**Figure 2-7:** Normalized Fe K-edge XANES spectra from a)  $\text{Y}_3\text{Al}_x\text{Fe}_{5-x}\text{O}_{12}$ , b)  $\text{Y}_3\text{Ga}_x\text{Fe}_{5-x}\text{O}_{12}$ , and c)  $\text{Y}_3\text{Al}_x\text{Ga}_y\text{Fe}_{5-x-y}\text{O}_{12}$  materials are shown. The change in intensity of the pre-edge region is shown in the inset of each plot. Arrows indicate the change in intensity that occur with increasing Al and Ga content. .... 38

**Figure 3-1:** Powder XRD patterns collected from  $\text{Y}_{3-z}\text{Ce}_z\text{AlFe}_4\text{O}_{12}$ . Figure 3-1 (a) represents set 1, (b) represents set 2, (c) represents set 3, and (d) represents set 4. (Set descriptions are given in table 3-1) ..... 45

**Figure 3-2:** Normalized Ce  $\text{L}_3$  XANES spectra from (a) set 1 ( $\text{Ce}^{4+}$  was used as starting material and was quenched in air), (b) set 2 ( $\text{Ce}^{3+}$  was used as starting material and was quenched in air), (c) set 3 ( $\text{Ce}^{3+}$  was used as starting material and was slow cooled in air), and (d) set 4 ( $\text{Ce}^{3+}$  was used as starting material and was slow cooled under  $\text{N}_2$ )..... 48

**Figure 3-3:** Normalized Ce  $\text{L}_3$ -edge XANES spectra from  $\text{Y}_{2.85}\text{Ce}_{0.15}\text{AlFe}_4\text{O}_{12}$  showing the change in Ce oxidation state that occurs depending on starting material. (a) Represents as-

synthesized samples annealed under the same conditions and then quenched in air directly from 1400°C. (b) Represents samples that were post- annealed at 800°C..... 49

**Figure 3-4:** Normalized Ce L<sub>3</sub>-edge XANES spectra from Y<sub>2.85</sub>Ce<sub>0.15</sub>AlFe<sub>4</sub>O<sub>12</sub> showing the change in Ce oxidation state that occurs depending on the annealing environment. All materials were synthesized using Ce(NO<sub>3</sub>)<sub>3</sub>·6H<sub>2</sub>O as the starting material. (a) Compares the spectra from the materials that were synthesized under N<sub>2</sub>(g) or air followed by slow cooling to room temperature. (b) Compares the spectra from the materials that were synthesized under N<sub>2</sub>(g) or air and then post-annealed at 800°C. .... 50

**Figure 3-5:** Normalized Ce L<sub>3</sub>-edge XANES spectra from Y<sub>2.85</sub>Ce<sub>0.15</sub>AlFe<sub>4</sub>O<sub>12</sub> showing the change in Ce oxidation state that occurs depending on the cooling rate used after high temperature annealing. All materials were synthesized using Ce(NO<sub>3</sub>)<sub>3</sub>·6H<sub>2</sub>O as the starting material. (a) Compares the spectra from the materials that were slow cooled to room temperature vs. those that were quenched in air from 1400 °C. (b) Compares the spectra from the materials that were post-annealed at 800°C. .... 51

**Figure 3-6:** Normalized Fe K-edge XANES spectra from (a) set 1 (Ce<sup>4+</sup> was used as starting material and was quenched in air), (b) set 2 (Ce<sup>3+</sup> was used as starting material and was quenched in air), (c) set 3 (Ce<sup>3+</sup> was used as starting material and was slow cooled in air), and (d) set 4 (Ce<sup>3+</sup> was used as starting material and was slow cooled under N<sub>2</sub>(g)). .... 54

**Figure A-1:** Normalized Ce L<sub>3</sub>-edge XANES spectra from Y<sub>2.80</sub>Ce<sub>0.20</sub>AlFe<sub>4</sub>O<sub>12</sub> showing the change in Ce oxidation state that occurs depending on the starting material. (a) The Ce L<sub>3</sub>-edge XANES spectra from the as-synthesized samples annealed under the same conditions and then quenched in air from 1400°C. (b) The Ce L<sub>3</sub>-edge XANES spectra from the samples that were post- annealed at 800°C. .... 69

**Figure A-2:** Normalized Ce L<sub>3</sub>-edge XANES spectra from Y<sub>2.80</sub>Ce<sub>0.20</sub>AlFe<sub>4</sub>O<sub>12</sub> showing the change in the Ce oxidation state that occurs depending on annealing environment. (a) The Ce L<sub>3</sub>-edge XANES spectra from the as-synthesized samples formed using the Ce<sup>3+</sup>-containing starting material that slow cooled to room temperature. (b) The Ce L<sub>3</sub>-edge XANES spectra from the samples that were post-annealed at 800°C..... 70

**Figure A-3:** Normalized Ce L<sub>3</sub>-edge XANES spectra from Y<sub>2.80</sub>Ce<sub>0.20</sub>AlFe<sub>4</sub>O<sub>12</sub> showing the change in the Ce oxidation state that occurs depending on the cooling rate used after high temperature annealing. (a) The Ce L<sub>3</sub>-edge XANES spectra from the as-synthesized samples

formed using the  $\text{Ce}^{3+}$ -containing starting material and the same annealing conditions. (b) The Ce  $\text{L}_3$ -edge XANES spectra from the samples that were post-annealed at  $800^\circ\text{C}$ ..... 70

## List of Abbreviations

APS	Advanced Photon Source
CLS	Canadian Light Source
CN	Coordination Number
EXAFS	Extended X-ray Absorption Fine Structure
HLW	High Level Waste
IAEA	International Atomic Energy Agency
ILW	Intermediate-level waste
$I_0$	Intensity of incident X-ray beam
$I_t$	Intensity of transmitted X-ray beam
$I_f$	Intensity of fluorescent photons
LLW	Low -level waste
PNC/XSD	Pacific Northwest Consortium/X-ray Science Division
SYNROC	Synthetic Rock
$t$	Sample thickness
TEY	Total Electron Yield
UHV	Ultra-high vacuum
VLS-PGM	Variable Line Spacing-Plane Grating Monochromator
XANES	X-ray Absorption Near-Edge Spectroscopy
XAS	X-ray Absorption Spectroscopy
XRD	X-ray Diffraction

$\mu$  Absorption Coefficient

$\theta$  Incident angle

# 1 Introduction

## 1.1 Introduction:

Balancing the growing demand for energy against global climate change is a challenge in the 21<sup>st</sup> century. Researchers have suggested that global electricity demand will double by 2050.<sup>1-</sup><sup>3</sup> The environmental threats from climate change are caused by anthropogenic CO<sub>2</sub> emission from fossil fuel resources (i.e., coal, oil, natural gas).<sup>4</sup> The continual use of non-renewable sources of energy (fossil fuels) will pose an imminent risk of exhausting the remaining fossil fuel supply.<sup>4-6</sup> Different forms of energy have gained attention as an alternative to fossil fuel to meet the energy demands of the present world.<sup>1,7,8</sup> Nuclear energy has been considered as a reliable and efficient alternative source. Nuclear energy has been proposed as a strategy to fight global warming and energy security since it offers significantly lower carbon emission than conventional fossil fuel plants.<sup>6,8,9</sup> Nuclear energy is a reliable and efficient energy source derived from the fission of an atom which can be used as a new source of energy to meet the growing energy requirements. The primary isotope used to produce nuclear energy is U-235 fuel, which allows it to provide more energy than fossil fuels.<sup>2,6</sup> As of 2010, Canada produced 15% of its electricity from 17 nuclear power reactors.<sup>10</sup> As of 2015, there were 442 reactors operating in the world, generating around 383GW of electricity.<sup>11</sup> However, radioactive waste produced from nuclear reactors need well developed disposal systems. Radioactive waste not only needs immobilization to separate it from the biosphere but also needs shielding and remote handling.<sup>12,13</sup> Many scientific studies have suggested the atomic level confinement of radioactive waste elements into amorphous or crystalline matrices.<sup>14,15</sup> Several types of nuclear wasteforms (i.e., glasses, ceramics, glass-ceramic composites) have been proposed for the sequestration of radioactive waste.<sup>16,17</sup> Chemical

durability, physical properties, and radiation resistance are very important parameters for these wasteforms to be considered as a host matrix for radioactive nuclides.<sup>14,18–20</sup> Therefore, investigations are currently in progress to develop new host matrices which can incorporate more radioactive waste for longer times. In order to design new solid-state materials as nuclear wasteforms, it is important to understand the host matrix and this thesis aims to address this aspect by detailing studies on the effect of substitution into crystalline solids (garnet) proposed for nuclear waste sequestration applications using X-ray based diffraction and spectroscopic techniques. Burakov *et al.* proposed that garnet type oxides can be a potential candidate for nuclear waste sequestration.<sup>21</sup> Garnet has recently been investigated as a potential host matrix for the immobilization of actinide elements found in high level nuclear waste due to the high chemical flexibility of this structure.<sup>21–30</sup> This chapter starts with a description of the garnet structure followed by a brief description of nuclear waste generation and management. The characterization techniques (e.g., X-ray diffraction and X-ray Absorption spectroscopy) used to study these materials are also briefly discussed. The main objectives of this thesis will be presented at the end of this chapter.

## 1.2 Crystal structure of garnet:

The garnet structure, originally solved by Menzer, has the general formula  $X_3A_2B_3O_{12}$  where X, A, and B indicate, respectively, the 8-coordinate dodecahedral, 6-coordinate octahedral, and 4-coordinate tetrahedral sites in the cubic system.<sup>31</sup> The X site is usually occupied by divalent, trivalent, and tetravalent elements, such as  $Ca^{2+}$ ,  $Ce^{3+}$ ,  $Ce^{4+}$ ,  $Th^{4+}$ , and  $U^{4+}$ . The A- and B-sites are occupied by trivalent and tetravalent elements (i.e.,  $Al^{3+}$ ,  $Fe^{3+}$ ,  $Si^{4+}$ , and  $Cr^{3+}$ ). The A-site (tetrahedra) and B-site (octahedra) form chains in the  $\langle 100 \rangle$  direction by sharing corners, and both share edges with the X-site to form a three-dimensional framework.<sup>32,33</sup> Materials adopting the



garnet-type structure have the space group  $Ia\bar{3}d$  with 8 formula units per unit cell. There are 160 atoms per unit cell and all oxygens are identical and are each bonded to one tetrahedron, one octahedron and to two of the dodecahedral sites. Oxygen lies in a special position and there are 96 per unit cell.

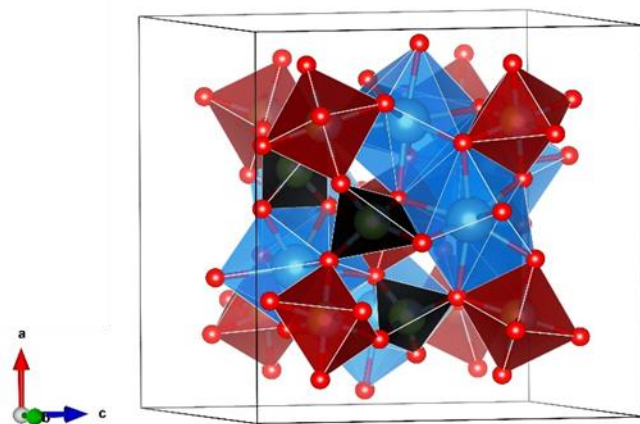


**Figure 1-1:** A schematic representation of the garnet structure is shown. Blue, red, and black polyhedra represent the 8-, 6-, and 4-coordinate sites, respectively. Red spheres represent the oxygen atoms.

### 1.3 Nuclear waste generation and management:

The management of radioactive waste has been a key challenge to generate nuclear power. Radioactive waste is a by-product from the operation of a nuclear reactor or from the reprocessing of spent nuclear fuel.<sup>5,6,17,20,34,35</sup> Nuclear power plants produce heat by nuclear fission in which an isotope, typically uranium ( $^{235}\text{U}$ ), transforms into lighter atoms upon bombardment with a neutron and releases large amounts of energy in the form of heat.<sup>36</sup> Naturally occurring uranium primarily consists of two isotopes namely U-238 (99.3%) and U-235 (0.7%) of which U-235 is the most fissile isotope.<sup>34,37–39</sup> There are plenty of different nuclear reactor designs but in general the reactor captures the released energy and uses it to heat up water into steam which runs through turbines

that spin generators.<sup>5,39</sup> A nuclear reactor generally consists of a fuel assembly, moderator, coolant, control rods, pressure vessel, and steam generator.<sup>5</sup> When fuel is used in a nuclear reactor, energy is released by the fission of actinides such as U-235 and Pu-239; this results in the build-up of fission products (e.g. Rb, Sr, Y, Zr, Nb, Mo, Tc, Ru, Cs) in the fuel.<sup>17</sup> Eventually, the continued irradiation of a fuel becomes uneconomical and it must be removed from the reactor. The waste resulting from this process are enriched with fission products (e.g., Rb, Sr, Y, Zr, Nb, Mo, Tc, Ru, Cs, Ce, Sm), impurities from the cladding material (e.g., Zr, Mo, Mg), corrosion products (e.g., Fe, Al, Co, Cr), transuranic elements (e.g., Np, Am, Cm), and process chemicals.<sup>22,40</sup>

Radioactive waste can be classified as low-level, intermediate-level, or high-level waste.<sup>10</sup> Classification of radioactive waste is based on the half-life of radionuclides.<sup>41</sup> Low-level nuclear waste (LLW) contains 90% of the volume but only 1% of the radioactivity of all nuclear waste.<sup>19,42</sup> Intermediate-level waste (ILW) contains higher amounts of radioactivity than low level waste and is comprised of chemical sludges, nuclear reactor parts, and contaminated materials from reactors.<sup>42</sup> High-level radioactive waste (HLW) produced either by the reprocessing of nuclear spent fuel or by nuclear weapons programs must be efficiently isolated from the biosphere. High level nuclear waste accounts for 95% of the total radioactivity generated in a nuclear reactor.<sup>41,43,44</sup> High-level waste is hazardous to humans and other life forms because high radiation levels are capable of producing fatal doses during short periods of direct exposure.<sup>16</sup>

In Canada, nuclear waste is stored in temporary storage facilities that will be used until a long-term solution is built.<sup>45</sup> As a temporary solution, the spent fuel rods are placed under water with continual monitoring for ~5-10 years.<sup>34</sup> The spent fuel rod, since it is still emitting radiation, continues to heat up the water, but the cooling systems and pumps keep the water below its boiling temperature.<sup>5,34</sup> Once the nuclear waste has cooled down enough in storage pools, it can be encased

in casks.<sup>20</sup> These concrete and steel containers (casks) block radiation, but this solution is far from permanent. Without proper maintenance, the casks could easily be damaged or breached over time and release radiation into the environment. Long-term nuclear waste storage needs to be situated in a geologically permanent environment without on-site supervision. The proposed strategy for completely isolating the waste from the biosphere is to permanently dispose the HLW in geologically stable underground locations.<sup>46</sup> HLW must be confined in solid and highly durable matrices that can ensure long-term stability and isolation before placing HLW in deep geological repositories.<sup>43</sup> The geological disposal of nuclear waste uses a multi-barrier concept, where the wasteform is one part which is surrounded by a container or a clay barrier (bentonite).<sup>43</sup> Both engineering and natural barriers are designed to prevent the radioactive waste from reaching the environment (biosphere).

Geological repositories are currently viewed by many to be one of the safest methods for the long-term storage of HLW.<sup>19,47</sup> Geological and environmental factors like ground water movement, erosion, flood, earthquake, and volcanic activities are important factors regarding disposal site selection.<sup>18</sup> Immobilization of radioactive waste in inert solid matrices before storage is beneficial for safety reasons. The selection of the immobilization technology depends on the physical and chemical nature of the waste and wasteform as well as the criteria for long-term storage and disposal facilities.<sup>48–50</sup>

### 1.3.1 Nuclear wasteforms:

Immobilisation is defined by the International Atomic Energy Agency (IAEA) as the conversion of a waste into a wasteform by solidification, embedding, or encapsulation.<sup>19,43,44,51,52</sup> The primary objectives of nuclear wasteforms are to provide greater resistance to leaching by groundwater and be capable of maintaining its structural integrity for a long period of time.<sup>44,53</sup> Solid matrices incorporating radionuclides are called nuclear wasteforms.<sup>14,15,50,54,55</sup> The wasteform represents the first and foremost barrier to the release of nuclear waste.<sup>56</sup> The functions of a wasteform are: to provide physical, chemical, and thermal stability, immobilization of the radioactive materials, and resistance against leaching, powdering, cracking, and other modes of degradation.<sup>43,56</sup>

A key concern for the nuclear wasteform are long-term stability and durability issues, which could be affected by the radioactive decay of incorporated nuclear waste elements.<sup>46,57,58</sup> The radiation is a result of radioactive decay of fission products via  $\beta$  ( $e^-$ ) particle emission.<sup>57</sup> Alpha particles ( $\alpha$ ;  $\text{He}^{2+}$ ) are produced from minor actinides.<sup>57</sup> When these radioactive nuclides are confined into a host material, the major effect that can influence the long-term stability of nuclear wasteforms is atomic displacements in the structure, which can result in the development of defects, swelling, and cracking of the material. Different nuclear wasteforms (i.e., amorphous, crystalline, combination of both) have been proposed based on the high waste loading, radiation stability, ease of processing, and physical and chemical durability of these materials.<sup>43,46,59–61</sup> Each nuclear wasteform offers unique features to incorporate nuclear waste elements, which will be discussed below.<sup>43,60,62</sup>

#### 1.3.1.1 Glass wasteforms:

The concept of using glass as a host for radioactive waste is based upon the radionuclides becoming part of the random three-dimensional glass network.<sup>46</sup> The immobilization of radioactive waste materials in glass is called vitrification.<sup>63,15,50,57,64</sup> The choice of composition for nuclear waste host glasses is a compromise between processability and wasteform durability.<sup>65</sup> Various glasses have been proposed as a nuclear wasteform based on their ability to accommodate a wide variety of waste-stream compositions, easy industrial processing, and radiation stability.<sup>50,66</sup> Borosilicate, phosphate, and rare-earth glasses have been proposed glass wasteforms to immobilize fission products and actinides.<sup>15,50,51</sup> However, depending on the composition of the glass wasteform, the waste loading capacities can be very poor (3-10 wt %) and the thermodynamic stability of nuclear waste glass is a concern for water contamination.<sup>17,43,50,67</sup> The interaction between a glass wasteform and ground water could potentially lead to the diffusion of radionuclides in the ground water.<sup>50</sup> Though the composition of glass wasteforms can vary significantly to match the desired application, the disadvantages of glass wasteforms (i.e., low waste loading; low thermal and chemical stability) have lead to the development of second generation wasteforms (crystalline wasteforms) for HLW immobilization applications.<sup>11,14,57</sup>

#### **1.3.1.2 Crystalline wasteforms:**

An ideal ceramic wasteform must have several different coordination polyhedra of various sizes and shapes to immobilize various radioactive nuclides. The use of crystalline wasteforms largely depends on the ability to incorporate a wide range of chemical species within their lattice.<sup>46</sup> Unlike glass wasteforms, radionuclides in crystalline ceramics occupy specific atomic sites and act as a part of the crystal structure.<sup>43,57</sup> Since the atomic sites in a crystal structure have specific size, charge, and bonding requirements, the crystalline host matrix imposes restrictions on the type of radioactive elements that can be incorporated into the crystal structure.<sup>43,68</sup> Crystalline

wasteforms have many potential advantages, such as high resistance to leaching and radiation damage, high waste loading, and excellent thermal and mechanical stability.<sup>46</sup> The advantages of ceramic wasteforms has led to the development of host ceramic structures for specific types of radioactive elements.<sup>53</sup>

Both single-phase and multi-phase crystalline ceramics have been proposed as host matrices for HLW. Multiphase ceramics (i.e., synroc) are multi-component mixtures of Ti-containing crystalline minerals like hollandite, perovskite, zirconolite, and rutile. Synroc was designed to immobilize multiple elements at the same time.<sup>44</sup> However, an expansion of one phase during radiation damage could induce cracking in an adjacent phase as well.<sup>44,49,50</sup> On the other hand, single phase crystalline wasteforms are tailored for specific radionuclides. Monazite, brannerite, pyrochlore, xenotime, and zircon are some of the proposed single-phase wasteforms.

Garnet has recently been investigated as a potential host matrix for the immobilization of actinide elements found in high level nuclear waste.<sup>22,69</sup> Natural uranium bearing garnet mineral such as Zr-containing elbrusite ( $\text{Ca}_3\text{UZrFe}_3\text{O}_{12}$ ; ~ 27 wt% U) , suggests that garnet has good long-term stability.<sup>70,71</sup> The high loading of U also suggests its great potential to be a waste host, which was also seen in synthetic garnets with up to ~ 30 wt% U under laboratory conditions.<sup>27,70-78</sup> Numerous studies have been completed on a wide range of compositions adopting the garnet structure to determine the capacity of these materials to incorporate actinides, as well as to determine the radiation resistance and stability in aqueous solutions of these materials.<sup>22,28,30,73</sup> The complex structure of garnet allows it to incorporate a large variety of elements with different oxidation states. In this thesis, the effect of chemical substitution on the garnet-type crystal structure has been studied using different techniques.

## 1.4 Experimental techniques:

Several techniques (i.e., powder X-ray diffraction, X-ray absorption near-edge spectroscopy) have been used in order to understand the structural changes in garnet type oxides. A brief overview of these technique is presented in the following section.

### 1.4.1 Powder X-ray diffraction (XRD):

Powder X-ray diffraction is an analytical technique used for phase identification of crystalline materials. This diffraction technique can provide information on phase purity, lattice parameters, atomic site positions, and crystallite size.<sup>79</sup> The analyzed power is finely ground, homogenized, and placed randomly with respect to the incident beam.<sup>79</sup>

When monochromatic X-rays beam fall onto a crystal lattice, some of the X-rays undergo coherent scattering without loss in energy. Diffraction occurs when light is scattered by a periodic array with long-range order, producing constructive interference at specific angles. This can be explained by applying Bragg's law of diffraction (shown in Figure 1-2). This law states that the path length difference ( $2d_{hkl}\sin\theta$ ) of the incident and the scattered X-rays of each lattice plane is an integral multiple of the wavelength ( $\lambda$ ) of the incident X-rays.

$$2d_{hkl}\sin\theta = n\lambda \quad (1.1)$$

Where ' $d_{hkl}$ ' is the spacing between the successive lattice planes, ' $\theta$ ' is the angle between the incident (or diffracted) beam and the lattice plane, ' $n$ ' is an integer, and ' $\lambda$ ' is the wavelength. For a crystalline material, the inter-planar distance of various lattice planes in a fixed wavelength can be measured by varying the angle between the diffracted beam and the lattice plane. Each structure has a set of unique d-spacings. Conversion of the diffraction peaks to d-spacings allows for the identification of the structure. Typically, this is achieved by comparison of d-spacings and

$2\theta$  values with standard reference patterns. The number and position of each diffraction peak depends on the lattice spacing, type, and parameters whereas the peak intensity depends on the type and position of the atoms within the structure. The width of the diffraction peaks can also provide information about the average crystallite size.

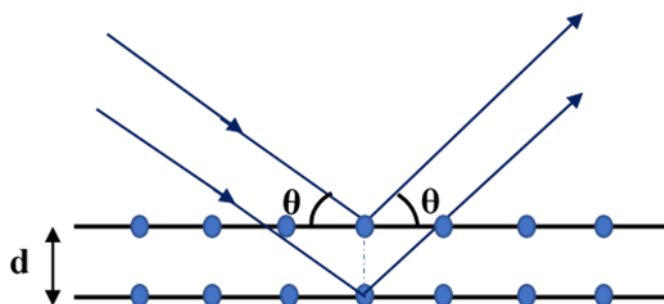


**Figure 1-2:** Schematic diagram of Bragg's law. When X-rays (wavelength,  $\lambda$ ) are incident on a lattice plane at an angle  $\theta$ , some of the X-rays undergo constructive interference.

#### 1.4.2 X-ray absorption spectroscopy (XAS):

In this thesis, X-ray absorption spectroscopy (XAS) has been used to probe the physical and electronic environments of the constituent elements in a material (e.g., coordination number, oxidation state).<sup>80</sup> XAS techniques require the use of a synchrotron facility, such as the Canadian Light Source (CLS) in Saskatoon, SK. Synchrotron facilities allow access to an extensive range of spectroscopic techniques because they can produce light across a large portion of the electromagnetic spectrum; from far-infrared light ( $\lambda < 15 \mu\text{m}$ ;  $E < 80 \text{ meV}$ ) to hard X-rays ( $\lambda < 30 \text{ pm}$ ;  $E > 40 \text{ keV}$ ).<sup>81–83</sup>

A simple schematic outlining the steps leading to the production of synchrotron radiation is shown in Figure1-3. Synchrotron radiation is produced when free electrons travelling near the speed of light are forced to take a circular trajectory via the application of a magnetic field and is



emitted in a direction that is tangential to the circular orbit of the electrons.<sup>84</sup> An electron gun is used to produce electrons via thermionic emission of electrons from a hot tungsten filament.<sup>81</sup> Then electrons enter into a linear accelerator, which is used to increase the energies of the electrons.<sup>85</sup> The higher energy electrons enter the booster ring travelling near the speed of light and get accelerated to even higher energies (i.e.; 250 MeV to 2.9 GeV).<sup>86,87</sup> Once the electrons are energized to GeV, they leave the booster ring and enter the storage ring. The storage ring consists of bending magnets and insertion devices, which are responsible for the generation of the most intense synchrotron radiation. Electrons circulation the storage ring generate very intense electromagnetic radiation.<sup>87-89</sup> The beamlines consist of energy tunable optical elements (e.g., grating and crystal monochromators) that enable the selection of electromagnetic radiation possessing specific wavelengths/energies.

### **1.4.3 X-ray Absorption Near-edge Spectroscopy (XANES):**

X-rays have sufficient energy to excite a core electron from an atom to the conduction or continuum states leaving an unoccupied core-hole state.<sup>84,90</sup> Since the absorption process involves a core electron excitation, XANES is element specific and sensitive to the oxidation state, bonding environment, and local geometry around the absorbing atom. An example of a XANES spectrum, the Fe K-edge from  $\text{Y}_3\text{Fe}_5\text{O}_{12}$ , is presented in Figure 1-4. The region starting just before the absorption edge and ending just after the absorption edge is often referred to as the near-edge region. The structure that is observed in the near-edge region can be referred as X-ray absorption near-edge spectroscopy. The oscillating features after the XANES region is defined as the extended X-ray absorption fine structure (EXAFS) region.

XANES spectra are sensitive to oxidation state and geometry while the EXAFS region is sensitive to the distances and distribution of electron density around the absorbing atom.<sup>81,88</sup> The

EXAFS region typically starts 20-30 eV above the edge jump.<sup>91-93</sup> When the ejected photoelectron wave scatters back on itself, the backscattered photoelectron wave can be in-phase or out-of-phase with the outgoing photoelectron wave.<sup>84,91-93</sup> As a result, the oscillation of photoelectron depends on the scattering power of the adjacent element present in the structure.<sup>84,93</sup> With proper analysis, the EXAFS region can be modeled to determine the interatomic distance, coordination number, and bond length.<sup>87,88</sup>

The XANES region shows pre-edge features and post-edge features, which are shown in Figure 1-4. These spectra are referenced by the principle quantum number ( $n$ ) of the electron being excited. The notation used to label X-ray absorption depends on the shell from which the electron is being excited, with K-, L-, and M-edges referring to the excitation of electrons from states with a principle quantum number of  $n = 1$ ,  $n = 2$ , and  $n = 3$ , respectively. In this work, L<sub>2,3</sub>- and K-edge XANES spectra were studied.

The energy at which the electron is excited is referred to as the absorption edge, and is identified by the principle quantum number of the electron being excited (e.g.,  $n = 1$  is the K-edge,  $n = 2$  is the L-edge, etc.). From the law of conservation of momentum, different electronic states can be probed separately because of the requirement to conserve the angular momentum that is imparted onto the electron when the photon is absorbed (Figure 1-5).<sup>81,84,94</sup> The excitation of the core electron generally follows the conservation of angular momentum,  $\Delta l = \pm 1$ , resulting in prominent dipolar electronic transitions (main edge features). However, weak quadrupolar transitions,  $\Delta l = \pm 2$ , are still observed (pre-edge features).<sup>84,95</sup> A first row element occupying tetrahedral cation sites has a strong mixing of 3d- and 4p-orbital which results from the loss of inversion symmetry.<sup>95,96</sup> In this case, quadrupolar transition can also occur along with the dipole transition but the intensity of the feature remains low (pre-edge region in Fig. 1-4).

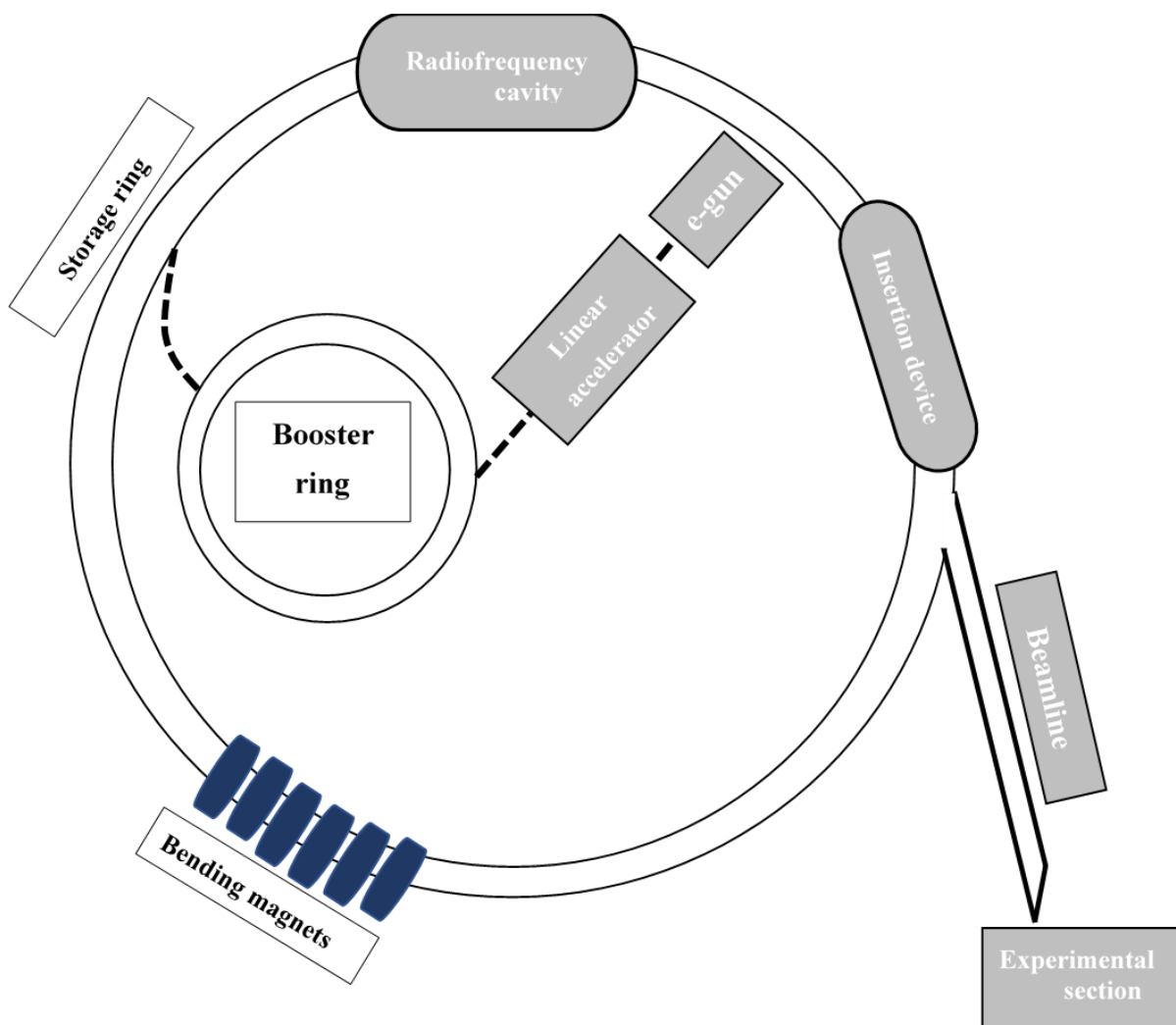


**Figure 1-3:** A schematic layout of a synchrotron radiation facility is presented. The electrons are accelerated to high energies using a linear accelerator. The electrons travel with a relativistic speed through the booster ring and storage ring maintaining a circular path. The storage ring consists of bending magnets and insertion devices, which are responsible for the generation of the most intense synchrotron radiation.

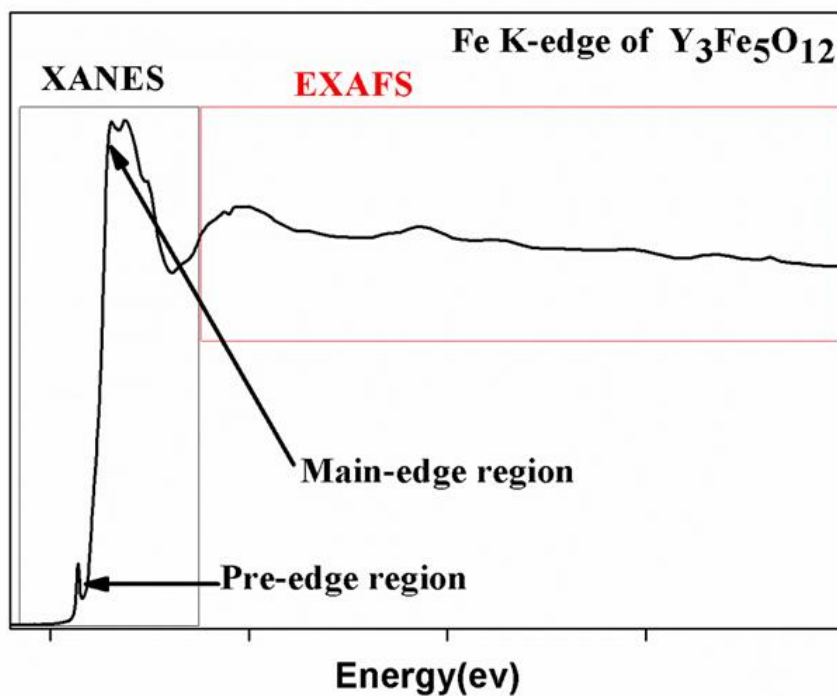


**Figure 1-4:** X-ray absorption spectrum from  $\text{Y}_3\text{Fe}_5\text{O}_{12}$ , showing the XANES and EXAFS regions. The XANES spectrum is further divided into pre-edge and main-edge regions.

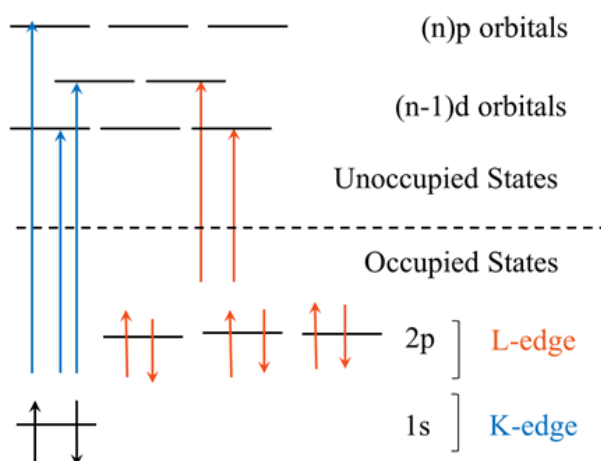


**Figure 1-5:** X-ray transitions commonly observed in the vicinity of metal K-edges include the dipole forbidden  $1s \rightarrow (n-1)d$  transitions, and the dipole allowed  $1s \rightarrow (n-1)p$ . L-edge includes dipole allowed  $2p \rightarrow ns$  and  $2p \rightarrow (n-1)d$  transitions.

During photo-excitation, the spin angular momentum of the remaining electron (not the excited electron) can align with or against its intrinsic orbital angular momentum, leading to different final state configurations.<sup>84</sup> As an example,  $\text{Al}^{3+}$   $L_{2,3}$ -XANES spectra is generated from  $2p \rightarrow 3s$  transitions. The p-states in L-shell splits into higher energy ( $2p_{1/2}$ ) and lower energy ( $2p_{3/2}$ ).<sup>92,97,98</sup> The  $L_2$ -edge ( $2p_{1/2} \rightarrow 3s$  or  $3d$ ) is always greater in energy than the  $L_3$ -edge ( $2p_{3/2} \rightarrow 3s$  or  $3d$ ).<sup>98,99</sup> The spherical symmetry of s-states preclude it from spin orbit coupling, so no splitting is observed in K-edge spectra.<sup>84,93,99,100</sup>

#### **1.4.4 Experimental Setup:**

The versatility of XANES is its ability to provide element-specific local structural information of a wide range of materials which includes, but is not limited to, crystalline, amorphous, and highly disordered materials.<sup>88,100</sup> In XANES, the measurement of absorption of X-rays by the sample is performed using multiple detection modes namely transmission, fluorescence, and electron yield.<sup>90,101</sup> Two different experimental setups were required to collect the XANES spectra presented in this thesis. One of them is transmission mode where the intensity of an X-ray beam is sampled before and after being transmitted through a sample (Figure 1-6) and the other one is fluorescence mode where a secondary emission from the absorption of an X-ray is measured.<sup>81</sup> The following sections describe the transmission setup for photon energies in the hard X-ray region and the ultra-high vacuum setup for photon energies in the soft X-ray region.

#### 1.4.4.1 Hard X-ray Transmission Experiments:

In transmission mode, the incident beam transmits through a sample and the X-ray beam is sampled before and after transmission is shown in Figure 1-6. The interaction of X-rays with matter can be described using Beer-Lambert law (Equation 1.2). In this equation,  $I_0$  represents the intensity of the incoming X-ray beam,  $I_t$  represents the intensity of the transmitted X-ray beam,  $\mu$  is the linear absorption coefficient, and  $t$  is the thickness of the sample.

$$I_t = I_0 e^{-\mu t} \dots\dots\dots(1.2)$$

The absorption of X-rays by the samples ( $\mu t$ ) is determined using the following equation:

$$\mu t = \ln \left( \frac{I_0}{I_t} \right) \dots\dots\dots(1.3)$$

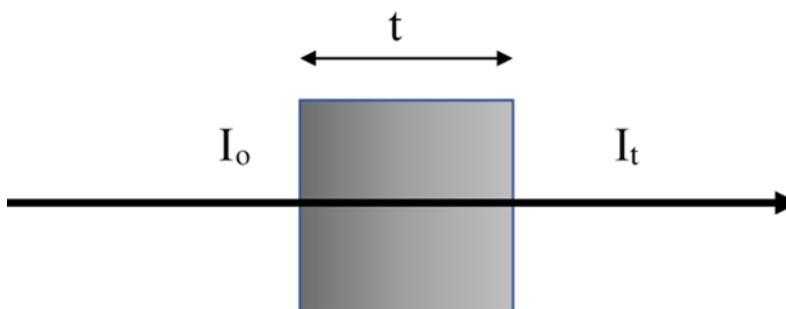


**Figure 1-6:** An incident beam of monochromatic X-ray with intensity  $I_0$  passes through a sample of thickness  $t$ . The transmission beam has intensity  $I_t$ . The absorption coefficient is followed by Beer-Lambert law.

The material has to be thin enough to transmit sufficient photon flux through the material to maintain a linear relationship between absorption and material thickness. This linear nature allows the background absorption from different materials to be scaled with respect to each other, resulting in spectra that represent the portion of the absorption coefficient solely from the element of interest for a given material. A typical experimental setup for hard X-ray XANES spectra is shown in Figure 1-7. The transmitted photon beam is measured in transmission mode since the beam passes through the entire thickness ( $t$ ) of the sample.<sup>94</sup>

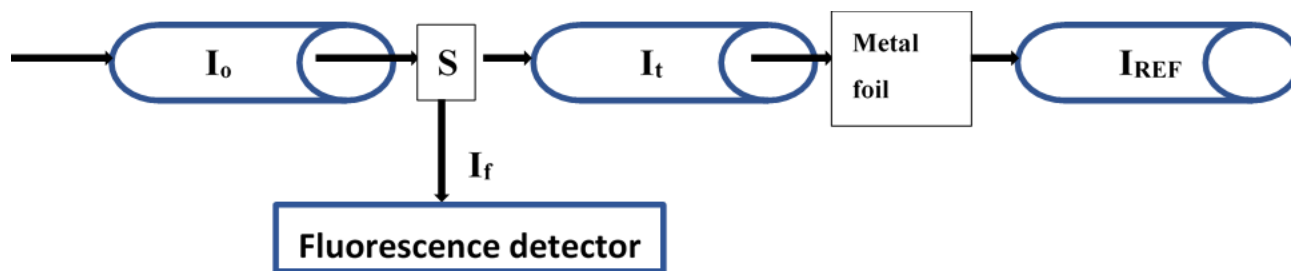


**Figure 1-7:** Hard X-ray transmission and fluorescence set-up. The X-ray photon beam from the ionization chamber ( $I_0$ ) is transmitted through the sample and the transmitted beam is measured using an ionization chamber ( $I_t$ ). The released fluorescence photons ( $I_f$ ) are collected using fluorescence detector.

X-rays with specific energies are obtained using a monochromator. The X-ray beam passes through an ionization chamber ( $I_0$ ) filled with inert gases (e.g.,  $N_2$ , Ar, He) wherein the X-rays ionize these gases. The intensity of the incident X-ray beam ( $I_0$ ) is determined by measuring the ionization current.<sup>81</sup> The X-rays after passing through the first ionization chamber are now incident on the sample and the absorption occurs when the energy of the X-rays is at or above the absorption edge of the element of interest. The transmitted X-rays pass through another ionization chamber wherein the intensity of the transmitted X-rays ( $I_t$ ) is determined. For calibration purposes, spectra are also collected from calibration standards placed between the transmission ( $I_t$ ) and reference ( $I_{REF}$ ) ionization chambers. Transmission experiments are ideally suited for measuring the absorption edges of elements in which the binding energy of the electrons falls in the hard X-ray regime. Due to the high energy of the X-rays, transmission experiments do not require ultra-high vacuum conditions (UHV) and are generally conducted under ambient conditions.

#### 1.4.4.2 Soft X-ray Fluorescent yield experiment:

In fluorescence mode, the incident X-ray photons sufficiently penetrate through the medium (small interaction with the matter) and the collected fluorescence photons escape from the bulk of the sample. The absorption coefficient is measured indirectly from fluorescence, which occurs when a higher energy electron core-level electron drops into an unoccupied lower energy state (Figure 1-8). In this experimental setup, powdered material is mounted to a sample plate and transferred into an ultra-high vacuum chamber.<sup>81</sup> This is because at lower X-ray energies, a fluorescent photon loses the majority of its energy via interactions with air molecules. A picture of an end station is shown below (Figure 1-9).

Fluorescence yield ( $I_f/I_o$ ) is proportional to the absorption by materials ( $\mu x$ ) as a function of incident angle ( $\theta$ ) of  $I_o$ . The equation is given below-

$$I_f/I_o \propto \mu x / \sin(\theta) \dots\dots\dots(1.4)$$



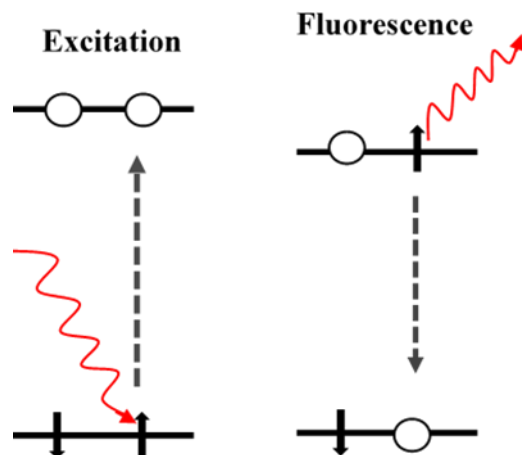


**Figure 1-8:** The excited atom leaves a core-hole (i.e., unoccupied state) while the electron in the excited state relaxes to lower energy to fill the core-hole.

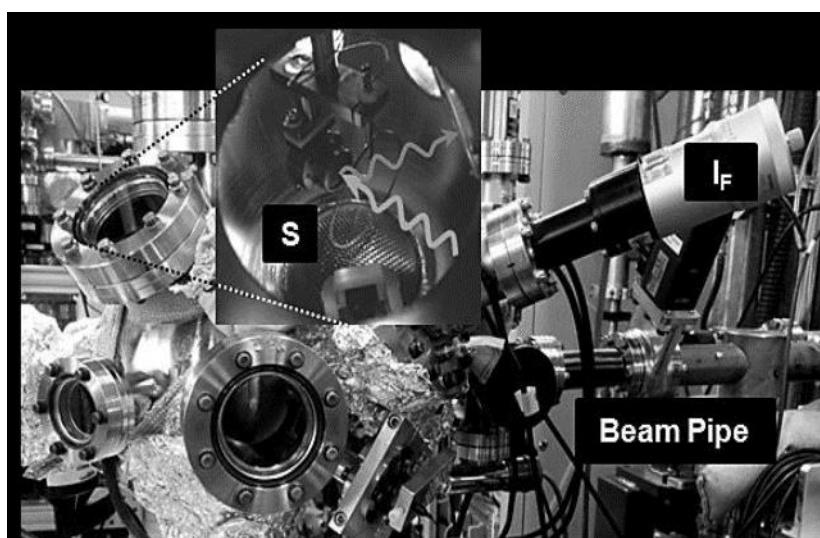


**Figure 1-9:** The ultra-high vacuum chamber for the VLS-PGM Beamline located at the Canadian Light Source in Saskatoon, SK. Entering via the beam pipe, the X-ray beam travels into the XAS chamber striking the sample (S), and the fluorescence ( $I_F$ ) signal is collected at a detector attached to one of the chamber ports.

## 1.5 Thesis overview:

The safe disposal of nuclear waste generated from nuclear reactors is critical to the environment. Criteria for the selection of proper hosts include chemical durability, waste loading,

radiation tolerance, and other properties related to their performance characteristics.<sup>11,43,58</sup> Garnet is a newly proposed material for nuclear waste sequestration, which has not been investigated robustly yet. Garnet has good chemical flexibility and its structure can accommodate actinides as well as other elements in variable oxidation states.<sup>27,74–76</sup> Many studies have suggested the large lattice dimensions of garnet (which allows it to accommodate large cations), high tetrahedral Fe content (which enhance the capacity to accommodate large ions), and high radiation resistance make it a suitable candidate for the sequestration of radioactive elements.<sup>27,30,70,72–76,102</sup> Despite the current level of understanding of garnet structures, there are some areas which have not been explored. For instance, crystalline materials can accommodate radioactive element in only certain specific sites. The radioactive nuclides are also sometimes accompanied by different corrosion products (Fe, Al, Ce, Cr). It is important to understand how the composition affects the site occupancies of materials, which is an important factor to enhance the capacity of garnet to incorporate radioactive nuclides. Further, substitution of U or Pu in garnet is complex because of their variable oxidation states. The main aim of this thesis is to study the change in local structure of garnet type oxide upon chemical substitution into dodecahedral, octahedral, and tetrahedral sites using powder X-ray diffraction and XANES. This thesis has two main objectives:

1. To understand how chemical substitution into octahedral and tetrahedral sites affects cation site disorder in garnet type oxides, which is discussed in Chapter 2.
2. To investigate the factors that affect the oxidation state of Ce incorporated into garnet type oxides using powder X-ray diffraction and X-ray absorption spectroscopy, which is discussed in Chapter 3.

## 2 Examination of the site preference in garnet type ( $X_3A_2B_3O_{12}$ ; $X=Y$ , $A/B=Al, Ga, Fe$ ) materials\*

### 2.1 Introduction:

The objective of this study was to determine how the occupancy of the A- and B-sites changes in primarily Fe-bearing garnet-type materials depending on composition. Four different series of garnet-type materials ( $Y_3Al_xGa_{5-x}O_{12}$ ,  $Y_3Al_xFe_{5-x}O_{12}$ ,  $Y_3Ga_xFe_{5-x}O_{12}$ , and  $Y_3Al_xGa_yFe_{5-x-y}O_{12}$ ) were synthesized under the same conditions and the local structures of the A- and B- sites were investigated to understand the site occupancies. Several studies have been performed to determine the metal site preference of  $Y_3Al_xGa_{5-x}O_{12}$ ,  $Y_3Al_xFe_{5-x}O_{12}$ , and  $Y_3Ga_xFe_{5-x}O_{12}$  materials using single crystal XRD and neutron diffraction methods.<sup>103–105</sup> However, quinary systems (e.g.,  $Y_3Al_xGa_yFe_{5-x-y}O_{12}$ ) where the A and B sites can contain up to three cations have not been extensively studied. It is difficult to determine the site occupancy of the A- and B-sites in quinary systems (e.g.,  $Y_3Al_xGa_yFe_{5-x-y}O_{12}$ ) based on the analysis of diffraction data alone. To resolve this, X-ray absorption near edge spectroscopy (XANES) has been used along with powder XRD to observe changes in the local structure in both quaternary and quinary garnet-type materials. XANES is element specific, and the coordination number (CN), charge, and bonding of the element of interest with neighboring atoms can be determined through the analysis of the absorption-edge energy and line shape of the spectra.<sup>84,95,97,106,107</sup>

In this study, both powder XRD and XANES have been used to understand the metal site preference of Al, Ga, and Fe in quaternary ( $Y_3Al_xGa_{5-x}O_{12}$ ,  $Y_3Al_xFe_{5-x}O_{12}$ , and  $Y_3Ga_xFe_{5-x}O_{12}$ ) and quinary ( $Y_3Al_xGa_yFe_{5-x-y}O_{12}$ ) systems. This study has not only identified how the Al, Ga, and Fe coordination number (CN) changes in quinary and quaternary systems, but has also further

---

\* A version of this Chapter has been published. The paper was reformatted to avoid repetition. Reprinted with the permission from Sifat, R., Grosvenor, A. P, Solid state sciences 83 (2018) 56-64. doi.org/10.1016/j.solidstatesciences.2018.06.013 21

established the usefulness of using both XANES and XRD to study the effect of composition on occupancies of different sites in crystal structures.

## **2.2 Experimental:**

### **2.2.1 Synthesis:**

The  $\text{Y}_3\text{Al}_x\text{Ga}_{5-x}\text{O}_{12}$ ,  $\text{Y}_3\text{Al}_x\text{Fe}_{5-x}\text{O}_{12}$ ,  $\text{Y}_3\text{Ga}_x\text{Fe}_{5-x}\text{O}_{12}$ , and  $\text{Y}_3\text{Al}_x\text{Ga}_y\text{Fe}_{5-x-y}\text{O}_{12}$  ( $0 \leq x \leq 5$ ;  $0 \leq y \leq 5$ ) materials were synthesized using the high temperature ceramic method under the same conditions. Stoichiometric amounts of  $\text{Al}_2\text{O}_3$  (Alfa Aesar; 98%),  $\text{Ga}_2\text{O}_3$  (Alfa Aesar; 99.99%),  $\text{Fe}_2\text{O}_3$  (Alfa Aesar; 99.945%), and  $\text{Y}_2\text{O}_3$  (Alfa Aesar; 99.99%) were mechanically mixed using a mortar and pestle and pressed into pellets at 6 MPa. These pellets were placed into alumina crucibles and heated at 1400 °C over 9 days before being quenched in air. Intermediate grinding and pelleting was performed on 3-days intervals to improve the homogeneity of the materials. Phase analysis of the materials was performed using powder XRD. The powder X-ray diffraction patterns were primarily collected using a PANalytical Empyrean diffractometer and a  $\text{Co K}_{\alpha 1,2}$  X-ray source although some XRD patterns were collected using an Inel diffractometer equipped with a  $\text{Cu K}_{\alpha 1}$  X-ray source. The lattice constants were determined using the PCW and Unitcell software programs.<sup>108</sup> A Rietveld refinement of the powder XRD patterns from the  $\text{Y}_3\text{Al}_x\text{Ga}_{5-x}\text{O}_{12}$  materials was completed to confirm the interpretation of the XANES spectra. The powder XRD patterns that were refined were collected in the  $2\theta$  range of  $10^\circ$  to  $120^\circ$  using the PANalytical XRD instrument mentioned above. Rietveld refinement was performed using the X'Pert HighScore Plus software program.<sup>109</sup> At first the background was determined followed by refining scale factor, zero shift, unit cell parameter, profile variable, and site occupancy, respectively. Other parameters were not allowed to vary while refining isotropic thermal factors at the very end. The atomic positions were

held constant during the refinement. The structural model used to fit these diffractograms was based on structure reported by Menzer.<sup>31</sup>

## **2.3 XANES**

### **2.3.1 Al L<sub>2,3</sub>- edge XANES:**

Al L<sub>2,3</sub>- edge XANES spectra were collected using the Variable Line Spacing Plane Grating Monochromator beamline (VLS- PGM, 11ID-2) located at the Canadian Light Source (CLS).<sup>83</sup> Samples were prepared by grinding them into fine powders and mounting them on carbon tape before being inserted into the ultra-high vacuum chamber. Fluorescence yield mode was used to collect XANES spectra using a 0.025 eV step through the absorption edge and an entrance slit of 50 x 50  $\mu\text{m}^2$ . The spectra were calibrated using Al metal the absorption edge energy set to 72.55 eV.<sup>101</sup>

### **2.3.2 Ga K- and Fe K-edge XANES:**

Fe K- and Ga K- edge XANES spectra were collected at the Advanced Photon Source (APS) using the Sector 20 bending magnet beamline (20-BM; CLS@APS) and a Si (111) crystal monochromator.<sup>101,110</sup> The Ga K-edge XANES spectra were collected using a 0.20 eV step through the absorption edge and the Fe K-edge XANES spectra were collected using a 0.15 eV step through the absorption edge. Samples were prepared by spreading a thin layer of finely ground powder between Kapton tape. The thickness was adjusted by adding or removing layers to ensure uniform absorption of X-rays by the materials. Ga metal was used as a reference for the Ga K-edge XANES spectra, with the absorption edge energy set to 10367 eV.<sup>83</sup> Fe metal foil was used as a reference, with the absorption edge energy set to 7112 eV for the Fe K-edge XANES spectra.<sup>83</sup> All spectra were calibrated, normalized, and analyzed using the Athena software program.<sup>110</sup>

## 2.4 Results and discussion:

### 2.4.1 Powder XRD:

Selected powder XRD patterns from the  $Y_3Al_xGa_{5-x}O_{12}$ ,  $Y_3Al_xFe_{5-x}O_{12}$ ,  $Y_3Ga_xFe_{5-x}O_{12}$ , and  $Y_3Al_xGa_yFe_{5-x-y}O_{12}$  materials are shown in Fig. 2-1. The XRD patterns are consistent with what would be expected from materials that adopt the garnet-type structure. The change in lattice constants depending on the composition of the quaternary materials are shown in Figure 2-2. The ionic radii of  $Al^{3+}$ ,  $Ga^{3+}$ , and  $Fe^{3+}$  in four coordinate-sites are 0.39Å, 0.47Å, and 0.49Å while the ionic radii of  $Al^{3+}$ ,  $Ga^{3+}$ , and  $Fe^{3+}$  in six coordinate-sites are 0.535Å, 0.62Å, and 0.69Å.<sup>111</sup> The lattice constants from the quaternary materials were observed to decrease linearly with increasing value of ‘x’ in the formula unit owing to the substitution of a larger cation for a smaller cation, which follows Vegard’s law.<sup>112</sup> The lattice constants for the quinary system ( $Y_3Al_xGa_yFe_{5-x-y}O_{12}$ ) are presented in Table 2-1. The observed lattice constants were observed to change depending on the change in Al, Ga, and Fe composition. The lattice constants were observed to decrease with increasing Al substitution while an increase was observed when the Ga or Fe concentrations increased. No linear trend was observed for the changes in the lattice constants from the  $Y_3Al_xGa_yFe_{5-x-y}O_{12}$  materials, indicating that Vegard’s law cannot be used to explain these changes.

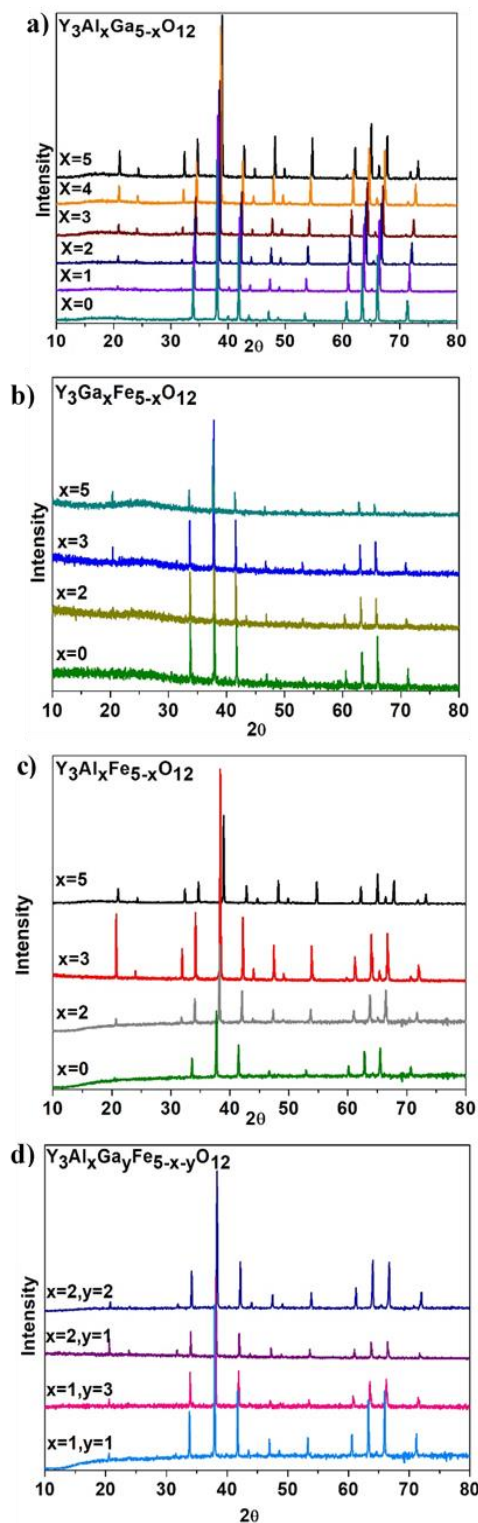


**Figure 2-1:** Normalized powder X-ray diffraction patterns collected from a)  $Y_3Al_xGa_{5-x}O_{12}$ , b)  $Y_3Ga_xFe_{5-x}O_{12}$ , c)  $Y_3Al_xFe_{5-x}O_{12}$ , and d)  $Y_3Al_xGa_yFe_{5-x-y}O_{12}$  are shown. The XRD patterns collected using a Cu source were converted to show how they would appear if a Co source was used for easy comparison between the four systems investigated.

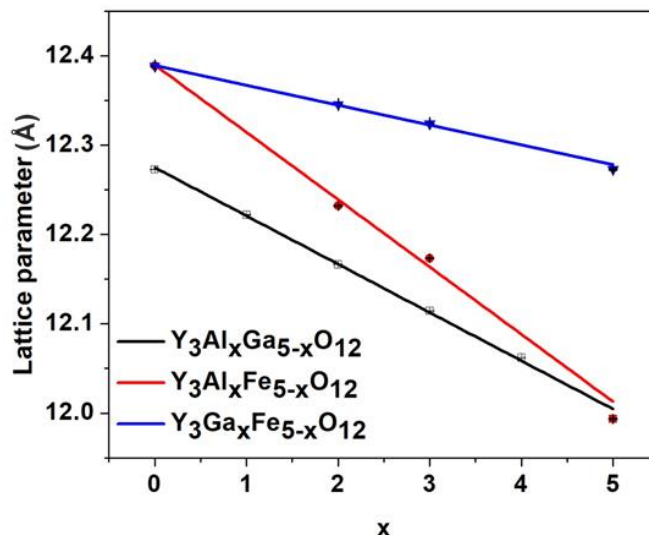


**Figure 2-2:** The change in lattice constant from the ternary systems is presented as a function of 'x'.

**Table 2-1:** Change in the lattice constants in the quinary (Y<sub>3</sub>Al<sub>x</sub>Ga<sub>y</sub>Fe<sub>5-x-y</sub>O<sub>12</sub>) system.

Change in x	Change in y	Composition	Lattice constant (Å)
x=1	y=1	Y <sub>3</sub> AlGaFe <sub>3</sub> O <sub>12</sub>	12.495(5)
x=1	y=3	Y <sub>3</sub> AlGa <sub>3</sub> FeO <sub>12</sub>	12.304(7)
x=2	y=1	Y <sub>3</sub> Al <sub>2</sub> GaFe <sub>2</sub> O <sub>12</sub>	12.227(5)
x=2	y=2	Y <sub>3</sub> Al <sub>2</sub> Ga <sub>2</sub> FeO <sub>12</sub>	12.183(4)

A Rietveld refinement of the powder XRD patterns collected from the Y<sub>3</sub>Al<sub>x</sub>Ga<sub>5-x</sub>O<sub>12</sub> materials was performed to develop an understanding of the site occupancy of Al<sup>3+</sup> and Ga<sup>3+</sup> in this system so as to validate the analysis of the XANES spectra presented below. The results of the Rietveld refinements are presented in Figure 2-3 and Table 2-2. It was observed that Al<sup>3+</sup> and Ga<sup>3+</sup> both occupy the O<sub>h</sub> and T<sub>d</sub> sites depending on composition. The ratio between octahedrally and tetrahedrally coordinated Al<sup>3+</sup> and between octahedrally and tetrahedrally coordinated Ga<sup>3+</sup>



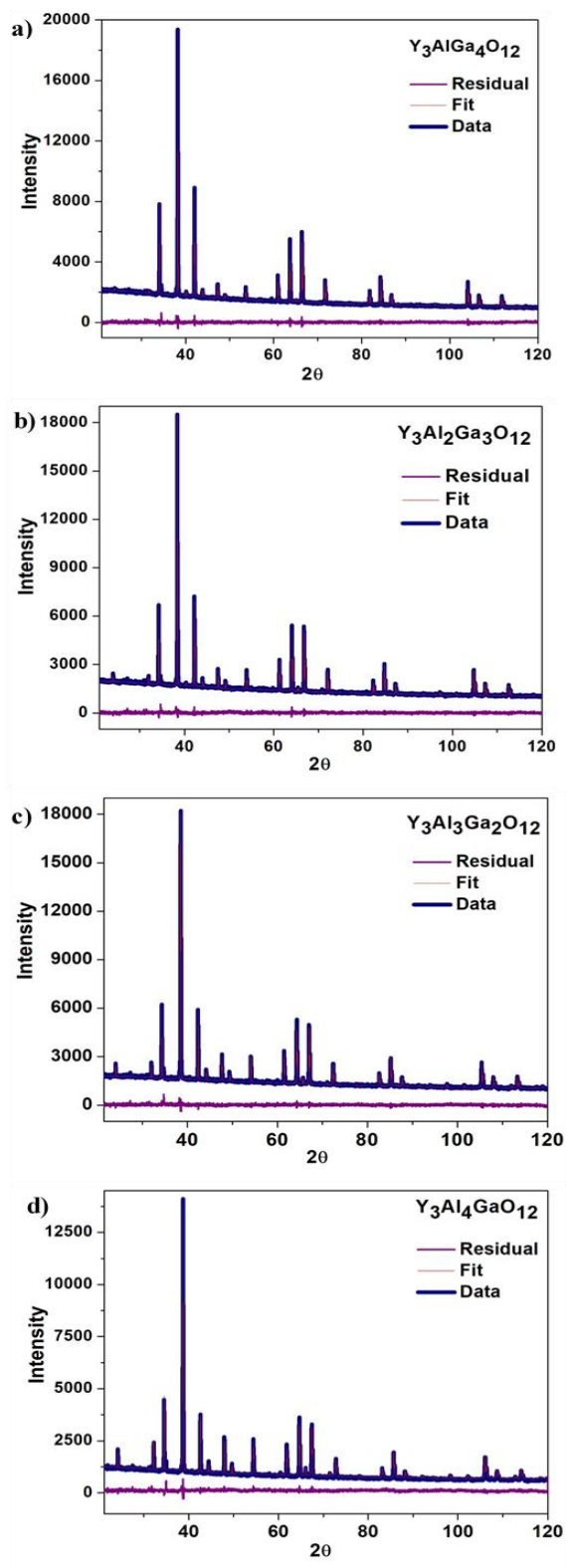


**Figure 2-3:** Results of the Rietveld refinement of powder XRD patterns from (a)  $Y_3AlGa_4O_{12}$ , (b)  $Y_3Al_2Ga_3O_{12}$ , (c)  $Y_3Al_3Ga_2O_{12}$ , and (d)  $Y_3Al_4GaO_{12}$  are presented.

are plotted against 'x' in Figure 2-4 and are also presented in Table 2-2. The largest  $O_h/T_d$  site occupancy ratio for  $Al^{3+}$  and  $Ga^{3+}$  were found for  $Y_3AlGa_4O_{12}$  and  $Y_3Ga_5O_{12}$ , respectively. As the  $Al^{3+}$  concentration increases with increasing 'x',  $Al^{3+}$  must also occupy the tetrahedral sites, resulting in the decreased value of the  $Al^{3+} O_h/T_d$  site occupancy ratio. On the other hand,  $Ga^{3+}$  was initially found to occupy both the octahedral and tetrahedral sites when the  $Al^{3+}$  concentration was low but was found to favour occupying the  $T_d$  site with increasing  $Al^{3+}$  concentration. The reasons for why  $Al^{3+}$  appears to favour occupying the octahedral site while  $Ga^{3+}$  appears to favour occupying the tetrahedral site are presented below during the discussion of the XANES results.

**Table 2-2: Rietveld refinement parameters for  $Y_3Al_xGa_{5-x}O_{12}$**

Parameters	$Y_3AlGa_4O_{12}$	$Y_3Al_2Ga_3O_{12}$	$Y_3Al_3Ga_2O_{12}$	$Y_3Al_4GaO_{12}$
Lattice Constant	12.21883(4) Å	12.16416 (4) Å	12.11021 (5) Å	12.05759(6) Å
<b>16a</b> occupancy (octahedral site)	Ga=0.690 (5) Al=0.310 (5)	Ga=0.449 (4) Al=0.551 (4)	Ga=0.262 (3) Al=0.738 (3)	Ga=0.103 (3) Al=0.897 (3)
<b>24d</b> occupancy (tetrahedral site)	Ga=0.864 (6) Al=0.136 (6)	Ga=0.683 (5) Al=0.317 (5)	Ga=0.472 (3) Al=0.528 (3)	Ga=0.240 (2) Al=0.760 (2)
<b>R<sub>expected</sub></b>	2.6991	2.6811	2.6795	3.4034
<b>R<sub>profile</sub></b>	2.9011	2.6863	2.5328	3.3300
Weighted <b>R<sub>profile</sub></b>	3.6319	3.3878	3.2056	4.1417
B overall	0.88(1)	0.73(1)	0.90(2)	0.84(2)

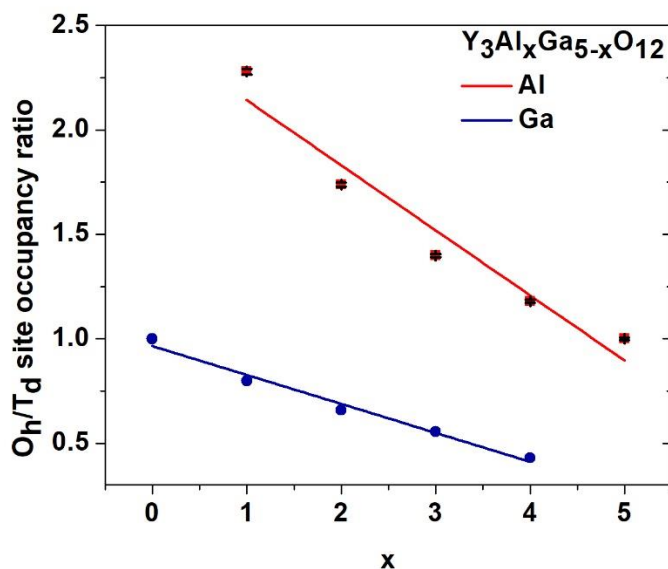


**Figure 2-4:** Change in Al<sup>3+</sup> and Ga<sup>3+</sup> O<sub>h</sub>/T<sub>d</sub> site occupancy ratio as a function of 'x'.

It is difficult to perform a Rietveld refinement of XRD patterns from quaternary systems like Y<sub>3</sub>Ga<sub>x</sub>Fe<sub>5-x</sub>O<sub>12</sub> because Ga (Z = 31) and Fe (Z = 26) have similar X-ray scattering factors.<sup>113</sup> Powder XRD patterns from quinary systems such as Y<sub>3</sub>Al<sub>x</sub>Ga<sub>y</sub>Fe<sub>5-x-y</sub>O<sub>12</sub> can also be difficult to refine owing to issues in determining the site occupancy of three different cations (Al<sup>3+</sup>, Ga<sup>3+</sup>, and Fe<sup>3+</sup>) over two different sites (O<sub>h</sub> and T<sub>d</sub>). XANES spectra were collected to overcome these issues so as to better understand how the average CN of Al<sup>3+</sup>, Ga<sup>3+</sup>, and Fe<sup>3+</sup> changes in Y<sub>3</sub>Al<sub>x</sub>Ga<sub>5-x</sub>O<sub>12</sub>, Y<sub>3</sub>Al<sub>x</sub>Fe<sub>5-x</sub>O<sub>12</sub>, Y<sub>3</sub>Ga<sub>x</sub>Fe<sub>5-x</sub>O<sub>12</sub>, and Y<sub>3</sub>Al<sub>x</sub>Ga<sub>y</sub>Fe<sub>5-x-y</sub>O<sub>12</sub> depending on composition.

## 2.5 XANES:

### 2.5.1 Al L<sub>2,3</sub>-edge XANES:

Al L<sub>2,3</sub>-edge XANES spectra were collected to better understand how the Al CN changes in the Y<sub>3</sub>Al<sub>x</sub>Ga<sub>5-x</sub>O<sub>12</sub>, Y<sub>3</sub>Al<sub>x</sub>Fe<sub>5-x</sub>O<sub>12</sub>, and Y<sub>3</sub>Al<sub>x</sub>Ga<sub>y</sub>Fe<sub>5-x-y</sub>O<sub>12</sub> systems depending on composition and are presented in Figure 2-5. The spectra result from the excitation of Al 2p electrons into unoccupied 3s- or 3d-states.<sup>114,115</sup> In Al containing compounds where Al has a single CN, the L<sub>3</sub>-

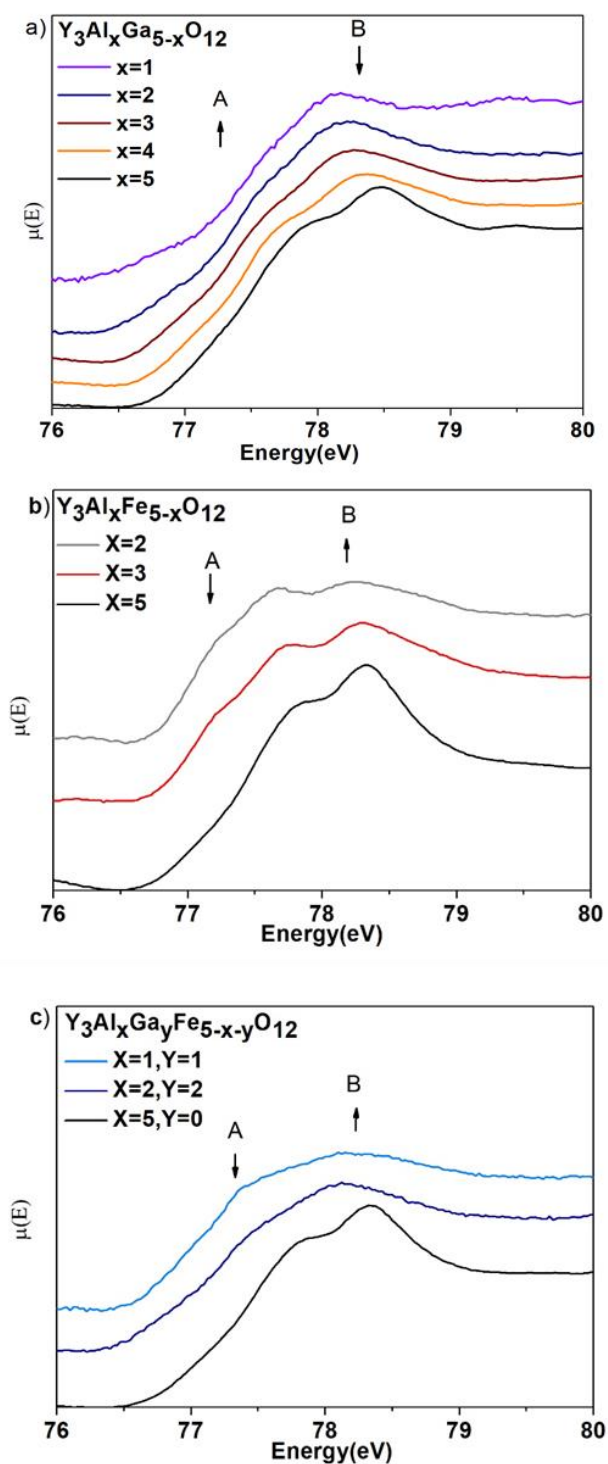


**Figure 2-5:** Normalized Al L<sub>2,3</sub>- edge spectra are presented from a)  $Y_3Al_xGa_{5-x}O_{12}$ , b)  $Y_3Al_xFe_{5-x}O_{12}$ , and c)  $Y_3Al_xGa_yFe_{5-x-y}O_{12}$ . Peak A corresponds to Al in the tetrahedral site while peak B corresponds to Al in octahedral site. Arrows indicate the change in intensity of peak A and peak B with increasing Al concentration.

and L<sub>2</sub>-edges can be resolved, with the onset energy of the absorption edge decreasing by ~1.5 eV as the CN of Al decreases from 6 to 4.<sup>115</sup> The core hole potential is screened less effectively as the number of anions (i.e., O<sup>2-</sup>) around the metal decreases, which results in a decrease of the final state energy and is observed as a decrease in the absorption energy. For spectra from materials that contain Al<sup>3+</sup> in both octahedral and tetrahedral environments, it has been demonstrated previously that the lower energy feature in the Al<sub>2,3</sub>-edge XANES spectrum (A in Figure 2-5) corresponds predominantly to tetrahedrally coordinated Al<sup>3+</sup> while the higher energy feature in the Al<sub>2,3</sub>-edge XANES spectrum (B in Figure 2-5) corresponds predominantly to octahedrally coordinated Al<sup>3+</sup>.<sup>114</sup>

The Al L<sub>2,3</sub>-edge XANES spectra from the Y<sub>3</sub>Al<sub>x</sub>Ga<sub>5-x</sub>O<sub>12</sub>, Y<sub>3</sub>Al<sub>x</sub>Fe<sub>5-x</sub>O<sub>12</sub>, and Y<sub>3</sub>Al<sub>x</sub>Ga<sub>y</sub>Fe<sub>5-x-y</sub>O<sub>12</sub> systems are presented in Figure 2-5. With increasing Al<sup>3+</sup> content in the Y<sub>3</sub>Al<sub>x</sub>Ga<sub>5-x</sub>O<sub>12</sub> system (Figure 2-5a), peak B was observed to decrease in intensity while peak A was observed to increase in intensity. This observation indicates that Al<sup>3+</sup> primarily occupies the octahedral site at low Al<sup>3+</sup> concentrations and that the amount of Al<sup>3+</sup> found in the tetrahedral site increases with increasing Al<sup>3+</sup> concentration. It should be noted that as Al<sup>3+</sup> is exchanged for Ga<sup>3+</sup>, the increase in intensity of peak A and the decrease in intensity of peak B does not indicate that Al<sup>3+</sup> occupies the octahedral site less. The change in intensity ratio of peak A and peak B is caused by the change in the relative amount of Al<sup>3+</sup> present in the tetrahedral and octahedral sites. An increase in the concentration of Al<sup>3+</sup> in Y<sub>3</sub>Al<sub>x</sub>Ga<sub>5-x</sub>O<sub>12</sub> forces Al<sup>3+</sup> to occupy the tetrahedral site as well as the octahedral site, resulting in a decrease in the average Al<sup>3+</sup> CN. These results are in agreement with the analysis of the Rietveld refinement of the XRD patterns from Y<sub>3</sub>Al<sub>x</sub>Ga<sub>5-x</sub>O<sub>12</sub>. Previous studies have proposed that the site preference of cations mainly depends on the ionic radius of the cations, crystal field stabilization, and the degree of interactions of the cation valence

s- and p-states with the anion.<sup>103,104,116</sup> The XANES and XRD data collected from the  $Y_3Al_xGa_{5-x}O_{12}$  system suggests that the larger  $Ga^{3+}$  cation (ionic radii [CN=6]: 0.69 Å) prefers to reside in the tetrahedral site while the smaller  $Al^{3+}$  cation (ionic radii [CN=6]: 0.535 Å) is found to predominantly reside in the octahedral site when the  $Al^{3+}$  concentration is low. The  $Al^{3+}$  and  $Ga^{3+}$  site occupancies in the  $Y_3Al_xGa_{5-x}O_{12}$  system can be explained by the nature of the bond between the cations and oxygen. In the case of  $Ga^{3+}$ , the observed tetrahedral site preference can be related to the presence of fully occupied Ga 3d orbitals (i.e.,  $3d^{10}$ ). Occupied 3d states in p-block elements result in a lowering of the energy of the conduction states. This contraction allows the bonding orbitals of Ga (4s and 4p) to overlap more with O bonding orbitals. This increase in covalent interaction between Ga and O bonding orbitals makes the metal more compressible and easier (compared to  $Al^{3+}$ ) to fit into the smaller tetrahedral site.<sup>103,114</sup> The valence states of  $Al^{3+}$  are higher in energy than those of  $Ga^{3+}$ , which results in a less effective overlap of Al 3s- and 3p-orbitals with O 2p-orbitals, favouring a more ionic bond.<sup>114,117,103</sup> As a result,  $Ga^{3+}$  preferentially occupies tetrahedral sites over  $Al^{3+}$ .

The Al  $L_{2,3}$ -edge XANES spectra from  $Y_3Al_xFe_{5-x}O_{12}$  (Figure 2-5b) show a decrease in intensity of peak A and increase in intensity of peak B with increasing Al content. It was demonstrated above during the analysis of the Al  $L_{2,3}$ -edge XANES spectra and XRD patterns from  $Y_3Al_xFe_{5-x}O_{12}$  that the strong preference of  $Ga^{3+}$  to occupy the  $T_d$  site forces  $Al^{3+}$  to reside in the octahedral site when the  $Al^{3+}$  concentration is low. However, analysis of the Al  $L_{2,3}$ -edge XANES spectra from the  $Y_3Al_xFe_{5-x}O_{12}$  system indicates that  $Al^{3+}$  primarily occupies the tetrahedral site in the  $Fe^{3+}$ -bearing materials, particularly when the  $Al^{3+}$  concentration is low. The larger  $Fe^{3+}$  cation (cationic radii [CN=6]: 0.69 Å) tends to reside more in the octahedral site while the smaller  $Al^{3+}$  cation (cationic radii [CN=6]: 0.535 Å) resides more in the tetrahedral site. Iron

having a 3+ oxidation state does not show any preference for occupying either tetrahedral or (high-spin) octahedral sites because of crystal field stabilization effects as the crystal field stabilization energy is zero for both coordination environments.<sup>118,119</sup> This, along with the observations presented above, indicates that the ionic radii differences between  $\text{Al}^{3+}$  and  $\text{Fe}^{3+}$  drives the site occupancies of the octahedral and tetrahedral sites in the  $\text{Y}_3\text{Al}_x\text{Fe}_{5-x}\text{O}_{12}$  system.

The Al  $L_{2,3}$ -edge XANES spectra from the quinary system ( $\text{Y}_3\text{Al}_x\text{Ga}_y\text{Fe}_{5-x-y}\text{O}_{12}$ ) are presented in Figure 2-5c. Analysis of the Al  $L_{2,3}$ -edge XANES spectra from the  $\text{Y}_3\text{Al}_x\text{Ga}_{5-x}\text{O}_{12}$  and  $\text{Y}_3\text{Al}_x\text{Fe}_{5-x}\text{O}_{12}$  systems (Fig. 2-5a and 2-5b) indicated that  $\text{Al}^{3+}$  does not show a specific preference for occupying either the octahedral or tetrahedral sites. With respect to the quinary system, the Al  $L_{2,3}$ -edge XANES spectra presented in Figure 2-5c shows that with increasing  $\text{Al}^{3+}$  content (and decreasing  $\text{Ga}^{3+}$  and  $\text{Fe}^{3+}$  concentration), the intensity of feature A decreases while the intensity of feature B increases. This result is similar to that observed for the  $\text{Y}_3\text{Al}_x\text{Fe}_{5-x}\text{O}_{12}$  system. The Al  $L_{2,3}$ -edge spectra from Figure 2-5c indicates as the Al concentration increases, the average CN of Al increases as well. Both Al and Ga replace Fe in the quinary ( $\text{Y}_3\text{Al}_x\text{Ga}_y\text{Fe}_{5-x-y}\text{O}_{12}$ ) system, and that substitution in the system gives rise to a competition factor among the three metals to reside into two polyhedra. The site preference of the metals (Al, Ga, and Fe) in the quinary system depends on their relative concentration in the system which will be discussed further later.

In general, the cation site distribution in these garnet type oxides has been found to be affected by cation size and the degree of interaction of the cation valence s- and p-orbitals with the anion bonding orbitals. The stronger covalency of the Ga-O bond compared to the Al-O bond is responsible for  $\text{Al}^{3+}$  being forced to primarily occupy the octahedral site in the  $\text{Y}_3\text{Al}_x\text{Ga}_{5-x}\text{O}_{12}$  system. With respect to the  $\text{Y}_3\text{Al}_x\text{Fe}_{5-x}\text{O}_{12}$  system, the site occupation is dominated by the size of the cations, which leads to the smaller  $\text{Al}^{3+}$  primarily occupying the tetrahedral site. For the

$\text{Y}_3\text{Al}_x\text{Ga}_y\text{Fe}_{5-x-y}\text{O}_{12}$  system, the site occupancy of  $\text{Al}^{3+}$  is affected by both cation size effects and the concentration of  $\text{Al}^{3+}$  in this material.

### 2.5.2 Ga K-edge XANES:

Ga K-edge XANES spectra were also collected from the  $\text{Y}_3\text{Al}_x\text{Ga}_{5-x}\text{O}_{12}$ ,  $\text{Y}_3\text{Ga}_x\text{Fe}_{5-x}\text{O}_{12}$ , and  $\text{Y}_3\text{Al}_x\text{Ga}_y\text{Fe}_{5-x-y}\text{O}_{12}$  systems. The normalized Ga K-edge XANES spectra, resulting from  $1s \rightarrow 4p$  transitions, are shown in Figure 2-6. The Ga K-edge XANES spectra show two main features which correspond to Ga occupying different coordination environments.<sup>120–122</sup> The lower energy feature (A in Figure 2-6) corresponds to tetrahedrally coordinated Ga and the higher energy feature (B in Figure 2-6) correspond to octahedrally coordinated Ga.<sup>117,120,122</sup> The Ga K-edge spectra shift to lower energy with decreasing CN for similar reasons as described in the previous section when discussing the Al  $L_{2,3}$ -edge XANES spectra.<sup>117,120,123</sup>

The normalized Ga K-edge XANES spectra from the  $\text{Y}_3\text{Al}_x\text{Ga}_{5-x}\text{O}_{12}$  system are shown in Figure 2-6a. As  $\text{Al}^{3+}$  was substituted for  $\text{Ga}^{3+}$ , the intensity of feature A was observed to increase while the intensity of feature B was observed to decrease. This observation indicates that the larger  $\text{Ga}^{3+}$  ion has a preference for residing in the tetrahedral site when the Ga concentration is low and only significantly occupies the octahedral site when the Ga concentration increases. These results are in agreement with the results from the Rietveld refinement of the powder XRD patterns and analysis of the Al  $L_{2,3}$ -edge XANES spectra from the  $\text{Y}_3\text{Al}_x\text{Ga}_{5-x}\text{O}_{12}$  system.

The normalized Ga K-edge XANES spectra from the  $\text{Y}_3\text{Ga}_x\text{Fe}_{5-x}\text{O}_{12}$  system are presented in Figure 2-6b. The intensity of the tetrahedral peak (peak A) was the most intense when the  $\text{Ga}^{3+}$  concentration was the lowest and was observed to decrease in intensity with a corresponding increase in the intensity of the octahedral peak (peak B) with increasing  $\text{Ga}^{3+}$  concentration. The



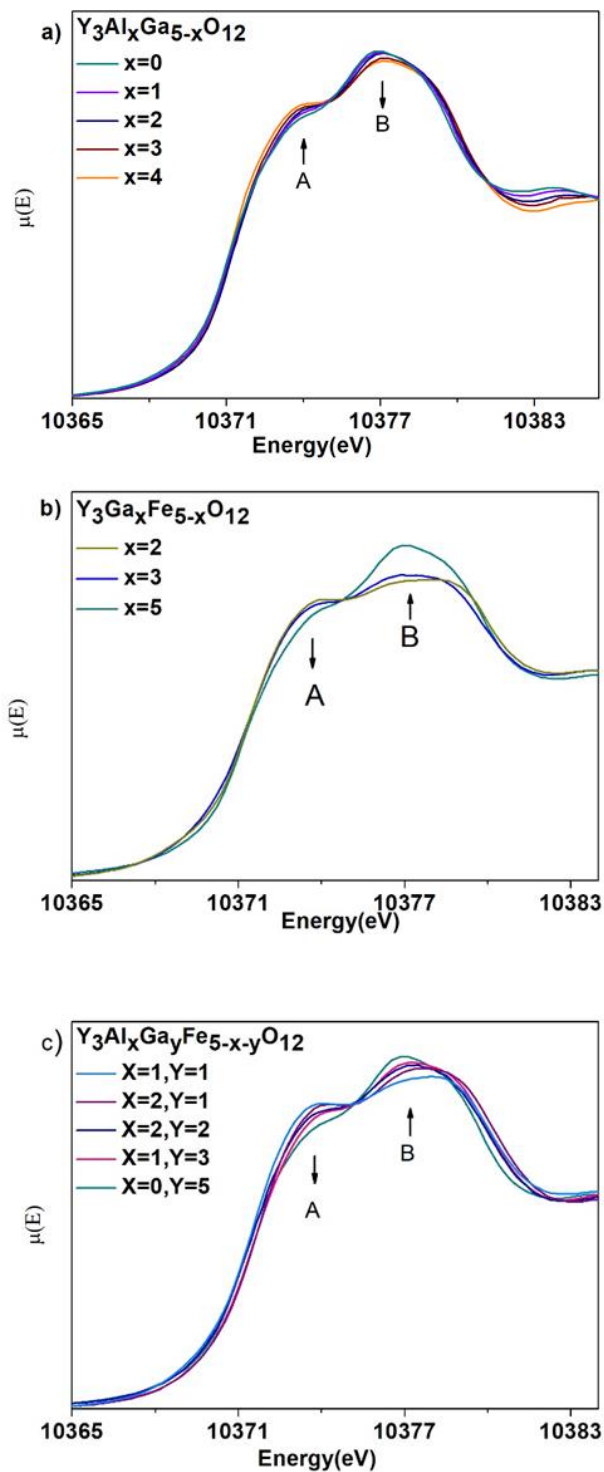


**Figure 2-6:** Normalized Ga K-edge from a)  $Y_3Al_xGa_{5-x}O_{12}$ , b)  $Y_3Ga_xFe_{5-x}O_{12}$ , and c)  $Y_3Al_xGa_yFe_{5-x-y}O_{12}$ . Peak A corresponds to  $Ga^{3+}$  in occupying the tetrahedral site and peak B corresponds to  $Ga^{3+}$  occupying the octahedral site. Arrows indicate the change in intensity of peak A and peak B with increasing 'x' (a) and (b) or 'y' (c)

observed decrease in intensity of the tetrahedral peak does not indicate that  $\text{Ga}^{3+}$  occupies the tetrahedral site less, instead, the change in intensity results from the change in the average CN of  $\text{Ga}^{3+}$  with increasing  $\text{Ga}^{3+}$  concentration. As noted above, it has been established previously that  $\text{Ga}^{3+}$  cations prefer to reside in tetrahedral sites vs. octahedral sites.<sup>103,120,121,123,124</sup> Further, the cation size difference between  $\text{Fe}^{3+}$  (ionic radii [CN=6]: 0.69Å) and  $\text{Ga}^{3+}$  (ionic radii [CN=6]: 0.67Å) is small. The analysis of the Ga K-edge XANES spectra from the  $\text{Y}_3\text{Ga}_x\text{Fe}_{5-x}\text{O}_{12}$  system has shown that the  $\text{Fe}^{3+}$  cations are forced to principally occupy the octahedral site because of the tetrahedral site preference of  $\text{Ga}^{3+}$  cations.

The normalized Ga K-edge XANES spectra from the quinary  $\text{Y}_3\text{Al}_x\text{Ga}_y\text{Fe}_{5-x-y}\text{O}_{12}$  system are presented in Figure 2-6c. These spectra show that with increasing Ga concentration, the intensity of peak A decreases while the intensity of peak B increases. It should be noted that the spectra have been normalized to each other. The intensity of feature A was observed to be the highest when the  $\text{Ga}^{3+}$  concentration was the lowest, indicating that  $\text{Ga}^{3+}$  preferentially occupies the tetrahedral site. The occupancy of the octahedral site was observed to increase with increasing  $\text{Ga}^{3+}$  concentration as can be observed in the Ga K-edge XANES spectra by an increase in the intensity of peak B.

Ga K-edge XANES spectra analysis from  $\text{Y}_3\text{Al}_x\text{Ga}_{5-x}\text{O}_{12}$ ,  $\text{Y}_3\text{Ga}_x\text{Fe}_{5-x}\text{O}_{12}$ , and  $\text{Y}_3\text{Al}_x\text{Ga}_y\text{Fe}_{5-x-y}\text{O}_{12}$  indicate that  $\text{Ga}^{3+}$  has a strong tetrahedral site preference as  $\text{Ga}^{3+}$  shows a strong preference for residing in the  $T_d$  site, it forces other metals ( $\text{Al}^{3+}$  and/or  $\text{Fe}^{3+}$ ) to occupy the octahedral sites. However,  $\text{Ga}^{3+}$  must occupy the octahedral site as well as the tetrahedral site when the concentration of  $\text{Ga}^{3+}$  increases in the system.

### 2.5.3 Fe K-edge XANES:

The normalized Fe K-edge XANES spectra from  $\text{Y}_3\text{Al}_x\text{Fe}_{5-x}\text{O}_{12}$ ,  $\text{Y}_3\text{Ga}_x\text{Fe}_{5-x}\text{O}_{12}$ , and  $\text{Y}_3\text{Al}_x\text{Ga}_y\text{Fe}_{5-x-y}\text{O}_{12}$  are shown in Figure 2-7. The spectra can be divided into two regions, the pre-edge region (feature A) and the main edge region (feature B). The pre-edge region (feature A) represents  $1s \rightarrow 3d$  transitions while the main-edge region (feature B) represents  $1s \rightarrow 4p$  transitions.<sup>95,125</sup> The intensity of the pre-edge region in the Fe K-edge XANES spectra is sensitive to changes in site disorder and coordination number. The pre-edge region results from a quadrupolar transition ( $1s \rightarrow 3d$  transitions), which is forbidden by the dipole selection rules that govern XANES spectra. However, a weak pre-edge features is still experimentally observed.<sup>95,97</sup> For centrosymmetric octahedral iron, electric dipole intensity cannot be gained by the mixing of 3d orbitals with the 4p orbitals but when inversion symmetry is lost and the Fe coordination decreases from 6 to 4, a greater mixing of Fe 4p- and 3d- states occurs. This mixing results in an increased dipole character of the pre-edge transition, leading to an increase in the intensity of the pre-edge region with decreasing coordination number.<sup>95,121</sup> The main-edge regions of transition metal K-edge spectra are also sensitive to changes in coordination number.<sup>125</sup> The intense main-edge region results from a dipole  $1s \rightarrow 4p$  excitation.<sup>96,117,126</sup> The intensity and energy of the main-edge region has been observed to decrease with decreasing CN.<sup>96,127,126</sup>

The normalized Fe K-edge XANES spectra from  $\text{Y}_3\text{Al}_x\text{Fe}_{5-x}\text{O}_{12}$  are presented in Figure 2-7a. As  $\text{Al}^{3+}$  was substituted for  $\text{Fe}^{3+}$ , the intensity of the pre-edge peak decreases while the intensity of the main-edge peak increases. This indicates that the  $\text{Fe}^{3+}$  CN is highest when the  $\text{Fe}^{3+}$  concentration is the lowest. It has been described earlier that the size of the cation is an important factor when determining the tetrahedral and octahedral site occupancies in the  $\text{Y}_3\text{Al}_x\text{Fe}_{5-x}\text{O}_{12}$

system. The analysis of the Fe K-edge XANES spectra confirm the site preference that was determined based on analysis of the Al L<sub>2,3</sub>-edge XANES spectra (Section 2.5.1).

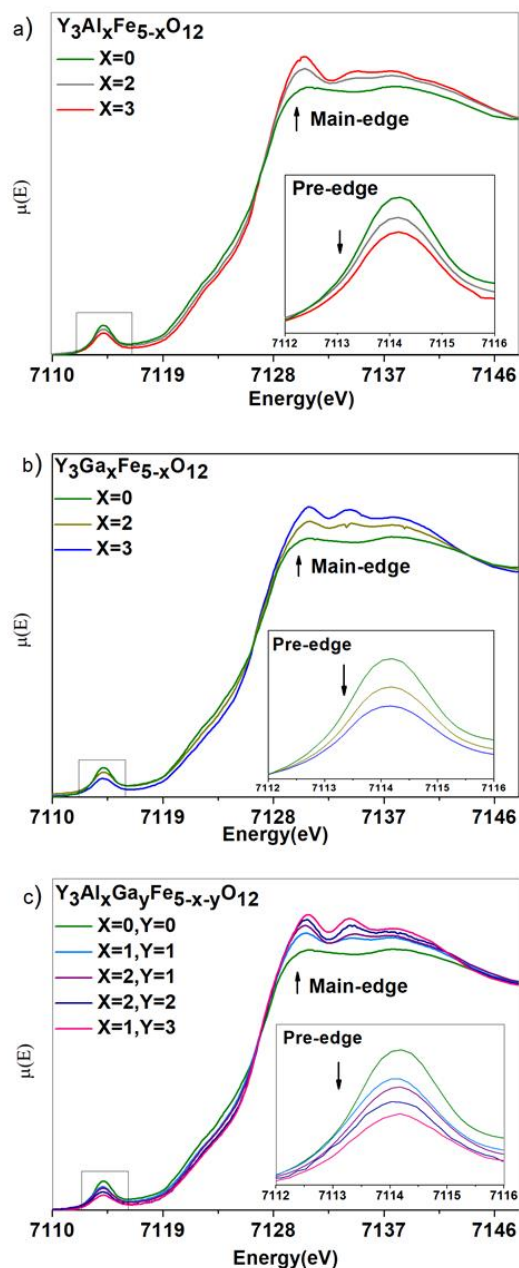


**Figure 2-7:** Normalized Fe K-edge XANES spectra from a)  $Y_3Al_xFe_{5-x}O_{12}$ , b)  $Y_3Ga_xFe_{5-x}O_{12}$ , and c)  $Y_3Al_xGa_yFe_{5-x-y}O_{12}$  materials are shown. The change in intensity of the pre-edge region is shown in the inset of each plot. Arrows indicate the change in intensity that occur with increasing Al and Ga content.

Normalized Fe K-edge XANES spectra from  $\text{Y}_3\text{Ga}_x\text{Fe}_{5-x}\text{O}_{12}$  are presented in Figure 2-7b. With increasing  $\text{Ga}^{3+}$  content, the main-edge feature increases and the pre-edge feature decreases, which is similar to the changes observed in the spectra from the  $\text{Y}_3\text{Al}_x\text{Fe}_{5-x}\text{O}_{12}$  system. These observations indicate that when the  $\text{Ga}^{3+}$  concentration is high,  $\text{Fe}^{3+}$  occupies the octahedral site more than the tetrahedral site as a result of the preference for  $\text{Ga}^{3+}$  to occupy the tetrahedral site. The analysis of the Fe K-edge XANES spectra are consistent with the analysis of the corresponding Ga K-edge XANES spectra presented in Section 2.52.

The normalized Fe K-edge XANES spectra from the quinary  $\text{Y}_3\text{Al}_x\text{Ga}_y\text{Fe}_{5-x-y}\text{O}_{12}$  system (Figure 2-7c) shows that as  $\text{Al}^{3+}$  and  $\text{Ga}^{3+}$  are substituted for  $\text{Fe}^{3+}$ , the intensity of the pre-edge region decreases while the intensity of the main-edge increases. This observation indicates that the average CN of  $\text{Fe}^{3+}$  increases with  $\text{Al}^{3+}$  and  $\text{Ga}^{3+}$  substitution in the system and is in agreement with the analysis of the Al  $L_{2,3}$ -edge (Section 2.5.1) and Ga K-edge (Section 2.5.2) XANES spectra collected from this system. The large  $\text{Fe}^{3+}$  cation radius and the preference for  $\text{Ga}^{3+}$  to occupy the tetrahedral site result in  $\text{Fe}^{3+}$  increasingly occupying the octahedral site in  $\text{Y}_3\text{Al}_x\text{Ga}_y\text{Fe}_{5-x-y}\text{O}_{12}$  with increasing  $\text{Al}^{3+}$  and  $\text{Ga}^{3+}$  substitution.

Fe K-edge XANES from  $\text{Y}_3\text{Al}_x\text{Fe}_{5-x}\text{O}_{12}$ ,  $\text{Y}_3\text{Ga}_x\text{Fe}_{5-x}\text{O}_{12}$  and  $\text{Y}_3\text{Al}_x\text{Ga}_y\text{Fe}_{5-x-y}\text{O}_{12}$  system show same site preference for Fe regardless of the substituted atoms. As mentioned earlier, crystal field stabilization effects cannot be used to determine the site preference of  $\text{Fe}^{3+}$  as the crystal field stabilization energy for this ion is zero for both coordination environments.<sup>118,119</sup> However, examination of the garnet-type oxides ( $\text{Y}_3\text{Al}_x\text{Fe}_{5-x}\text{O}_{12}$ ,  $\text{Y}_3\text{Ga}_x\text{Fe}_{5-x}\text{O}_{12}$  and  $\text{Y}_3\text{Al}_x\text{Ga}_y\text{Fe}_{5-x-y}\text{O}_{12}$ ) studied here has found that  $\text{Fe}^{3+}$  ions are primarily found to occupy the octahedral site. This implies that other factors (e.g., concentration and cation radius) affect the site occupancy of  $\text{Fe}^{3+}$  in these ferrite garnet-type oxides.<sup>96,117</sup>

## 2.6 Conclusions:

Synthetic garnet (depending on the composition) can accommodate U and Th into dodecahedral and octahedral sites.<sup>23,28</sup> The garnet structure can also be a suitable host for immobilization of actinide waste enriched with corrosion products (Fe, Al, Co, Cr).<sup>22,40</sup> As such, it is important to understand how the composition affects the site occupancies of materials adopting this structure as this may affect the amount of waste elements (often reported in wt%) that can be incorporated in the garnet structure. The study has shown how the metal site occupancies in a quinary garnet system ( $\text{Y}_3\text{Al}_x\text{Ga}_y\text{Fe}_{5-x-y}\text{O}_{12}$ ) and three quaternary systems ( $\text{Y}_3\text{Al}_x\text{Ga}_{5-x}\text{O}_{12}$ ,  $\text{Y}_3\text{Ga}_x\text{Fe}_{5-x}\text{O}_{12}$ ,  $\text{Y}_3\text{Al}_x\text{Fe}_{5-x}\text{O}_{12}$ ) change depending on the concentration of  $\text{Al}^{3+}$ ,  $\text{Ga}^{3+}$ , and  $\text{Fe}^{3+}$ . The factors that affect the site occupancies in the quinary and quaternary systems have also been discussed. The change in average coordination number of  $\text{Al}^{3+}$ ,  $\text{Ga}^{3+}$ , and  $\text{Fe}^{3+}$  in the quinary and quaternary systems has been analyzed by analysis of XRD patterns and XANES spectra. Analysis of the Fe K-, Ga K-, and Al L<sub>2,3</sub>- edge spectra confirm that  $\text{Ga}^{3+}$  prefers to reside in the four-coordinate tetrahedral site despite its large effective cationic radius compared to  $\text{Al}^{3+}$  or  $\text{Fe}^{3+}$ . The site occupancies of  $\text{Al}^{3+}$ ,  $\text{Ga}^{3+}$ , and  $\text{Fe}^{3+}$  in the garnet system are affected by different factors, including: the degree of interactions of the cation valence s- and p-states with the anion, concentration, and cation radius. All three factors are found to contribute to the site occupancies observed in the quinary system.

### 3 Investigation of the factors affecting the oxidation state of Ce in the garnet structure\*

#### 3.1 Introduction:

In chapter 2, the metal site occupancies in a quinary garnet system ( $Y_3Al_xGa_yFe_{5-x-y}O_{12}$ ) and three quaternary systems ( $Y_3Al_xGa_{5-x}O_{12}$ ,  $Y_3Ga_xFe_{5-x}O_{12}$ ,  $Y_3Al_xFe_{5-x}O_{12}$ ) have been discussed depending on the concentration of  $Al^{3+}$ ,  $Ga^{3+}$ , and  $Fe^{3+}$ . The garnet structure ( $X_3A_2B_3O_{12}$ ) has three types of cation polyhedra: a dodecahedral X-site, an octahedral A-site, and a tetrahedral B-site. It has been found that, among these three polyhedra, the eight-coordinate X site and six coordinate A-site can be occupied by large divalent, trivalent, and tetravalent cations (e.g., Ca, Ce, Th, and U).<sup>22,26,27,30,102</sup> Studies of natural uranium-bearing garnet minerals such as Zr-containing elbrusite ( $Ca_3UZrFe_3O_{12}$ ; ~ 27 wt% U) suggest that the garnet-type structure has good long-term stability.<sup>71</sup> The high loading of U within this phase also suggests the potential of materials adopting the garnet-type structure to be nuclear waste forms. It is notable that garnet has been synthesized that contains a high concentration of U (~30 wt. % U).<sup>22,128,129</sup> A considerable amount of work has been completed to study the stability of actinides in garnet against radiation damage and corrosion resistance.<sup>24,26,28,76</sup> However, factors that affect the change in oxidation states in garnet type oxides have not been addressed. It is also important to study the ability of a nuclear wasteform to incorporate radioactive actinides with variable oxidation states.<sup>24,27,74,78,130</sup> Substitution of U or Pu in garnet is complex because of their variable oxidation states. Since Ce can be considered as an analogue of different actinide elements (e.g., Pu).<sup>131,132</sup>

The objective of this investigation was to understand the effect of substituting Ce with different oxidation states into the X-site in the garnet-type structure. Four different sets of garnet ( $Y_{3-z}Ce_zAlFe_4O_{12}$ ;  $0.05 \leq z \leq 0.20$ ) materials were synthesized followed by analysis of powder X-

---

\* A version of this Chapter has been submitted for publication.

ray diffraction (XRD) patterns and X-ray absorption near-edge spectroscopy (XANES) spectra to study the effect of starting material, annealing temperatures, cooling rates, and annealing environments on the crystal structure and electronic structure of these materials. Ce L<sub>3</sub>- and Fe K-edge XANES spectra were collected to study how the Ce and Fe oxidation states changed in this system and to investigate if changes in the local structure occur.

## **3.2 Experimental:**

### **3.2.1 Synthesis and Powder XRD:**

The  $Y_{3-z}Ce_zAlFe_4O_{12}$  ( $0 \leq z \leq 0.20$ ) materials were prepared using the traditional ceramic method. Four sets of samples were synthesized using differing starting materials, annealing conditions, and cooling rates after high temperature annealing. Details of the synthesis of the four different sets of garnet materials are presented in Table 3-1. Stoichiometric amount of CeO<sub>2</sub> (Alfa Aesar; 99.9%), Al<sub>2</sub>O<sub>3</sub> (Alfa Aesar; 98%), Fe<sub>2</sub>O<sub>3</sub> (Alfa Aesar; 99.945%), and Y<sub>2</sub>O<sub>3</sub> (Alfa Aesar; 99.99%) were mixed and then heated under air at 1400 °C to produce samples for set 1. The materials were held at 1400 °C for 9 days with intermittent quenching, grinding, and re-pelleting. Once the reaction was complete, the samples from set 1 were quenched in air. As indicated in Table 3.1, stoichiometric amounts of Ce(NO<sub>3</sub>)<sub>3</sub>·6H<sub>2</sub>O (Alfa Aesar; 99.5%), Al<sub>2</sub>O<sub>3</sub> (Alfa Aesar; 98%), Fe<sub>2</sub>O<sub>3</sub> (Alfa Aesar; 99.945%), and Y<sub>2</sub>O<sub>3</sub> (Alfa Aesar; 99.99%) were used as starting materials for set 2, set 3, and set 4. The annealing environment and cooling rates after annealing were the same for set 1 and set 2. Samples from set 3 were annealed under air at 1400 °C and then slow cooled to room temperature, while samples from set 4 were annealed at 1400 °C under N<sub>2</sub>(g) (Praxair; 99.995%) and then slow cooled to room temperature under the same conditions.

The starting materials were mechanically mixed in appropriate stoichiometries using a mortar and pestle and pressed into pellets at 6 MPa. The pellets were heated at 1400 °C under different conditions (depending on set) for 9 days and then cooled to room temperature using



different cooling rates. Intermediate grinding and pelleting was performed on 3-day intervals to improve the homogeneity of the materials. Two samples from each set were post annealed (PA) at 800°C for 48 hours followed by the cooling rate assigned for each set. Phase analysis of the materials was performed using powder XRD. The powder X-ray diffraction patterns were collected using a Rigaku Ultima IV powder diffractometer with a Cu K $\alpha$  X-ray source.

**Table 3-1:** Labels and descriptions of different samples studied-

Assigned set no.	Starting materials	Annealing condition at 1400°C	Cooling rate after annealing
<b>Set 1</b>	CeO <sub>2</sub> , Al <sub>2</sub> O <sub>3</sub> , Fe <sub>2</sub> O <sub>3</sub> , and Y <sub>2</sub> O <sub>3</sub>	Annealed under air	Quenched in air
<b>Set 2</b>	Ce(NO <sub>3</sub> ) <sub>3</sub> .6H <sub>2</sub> O, Al <sub>2</sub> O <sub>3</sub> , Fe <sub>2</sub> O <sub>3</sub> , and Y <sub>2</sub> O <sub>3</sub>	Annealed under air	Quenched in air
<b>Set 3</b>	Ce(NO <sub>3</sub> ) <sub>3</sub> .6H <sub>2</sub> O, Al <sub>2</sub> O <sub>3</sub> , Fe <sub>2</sub> O <sub>3</sub> , and Y <sub>2</sub> O <sub>3</sub>	Annealed under air	Slow cooled to room temperature
<b>Set 4</b>	Ce(NO <sub>3</sub> ) <sub>3</sub> .6H <sub>2</sub> O, Al <sub>2</sub> O <sub>3</sub> , Fe <sub>2</sub> O <sub>3</sub> , and Y <sub>2</sub> O <sub>3</sub>	Annealed under N <sub>2</sub>	Slow cooled to room temperature

### 3.2.2 X-ray absorption near-edge spectroscopy (XANES):

Ce L<sub>3</sub>-edge and Fe K-edge XANES spectra were collected at the Advanced Photon Source (APS) using the Sector 20 bending magnet beamline (20-BM; CLS@APS) and a Si (111) crystal monochromator.<sup>101,110</sup> All spectra were collected using an energy step size of 0.15 eV/step through the absorption edge. Cr metal was used as a reference for the Ce L<sub>3</sub>-edge XANES spectra, with the absorption edge energy set to 5723 eV.<sup>83</sup> Fe metal foil was used as a reference with the absorption edge energy set to 7112 eV for the Fe K-edge XANES spectra.<sup>83</sup> The resolution of the

spectra was 0.8 eV at 5723 eV (Ce L<sub>3</sub>-edge) and 0.9 eV at 7112 eV (Fe K-edge). Samples were prepared by spreading a thin layer of finely ground powder between Kapton tape.<sup>101</sup> The thickness was adjusted by adding or removing layers to ensure uniform absorption of X-rays by the materials. Multiple scans were collected in both fluorescence yield and transmission mode. The transmission spectra were collected using an ionization chamber filled with 100% N<sub>2</sub> gas to achieve optimal absorption-edge heights. All spectra were calibrated, normalized, and analyzed using the Athena software program.<sup>110</sup>

### **3.3 Results and discussion:**

#### **3.3.1 Powder XRD:**

Powder XRD patterns were collected from all synthesized samples. Formation of phase-pure garnet-type oxides was confirmed for the Y<sub>3-z</sub>Ce<sub>z</sub>AlFe<sub>4</sub>O<sub>12</sub> ( $0 \leq z \leq 0.20$ ) materials, and no secondary phases were detected. Excess CeO<sub>2</sub> was detected in the samples when 'z' was > 0.20. The collected XRD patterns are shown in Figure 3-1. Post annealing of the materials at 800 °C was conducted to observe the effect of temperature on the Ce oxidation state and the collected XRD patterns from these post-annealed phases showed no significant changes in the patterns compared to the patterns from the as-synthesized materials. All patterns are representative of those expected from materials that adopt the garnet-type structure having a similar composition.

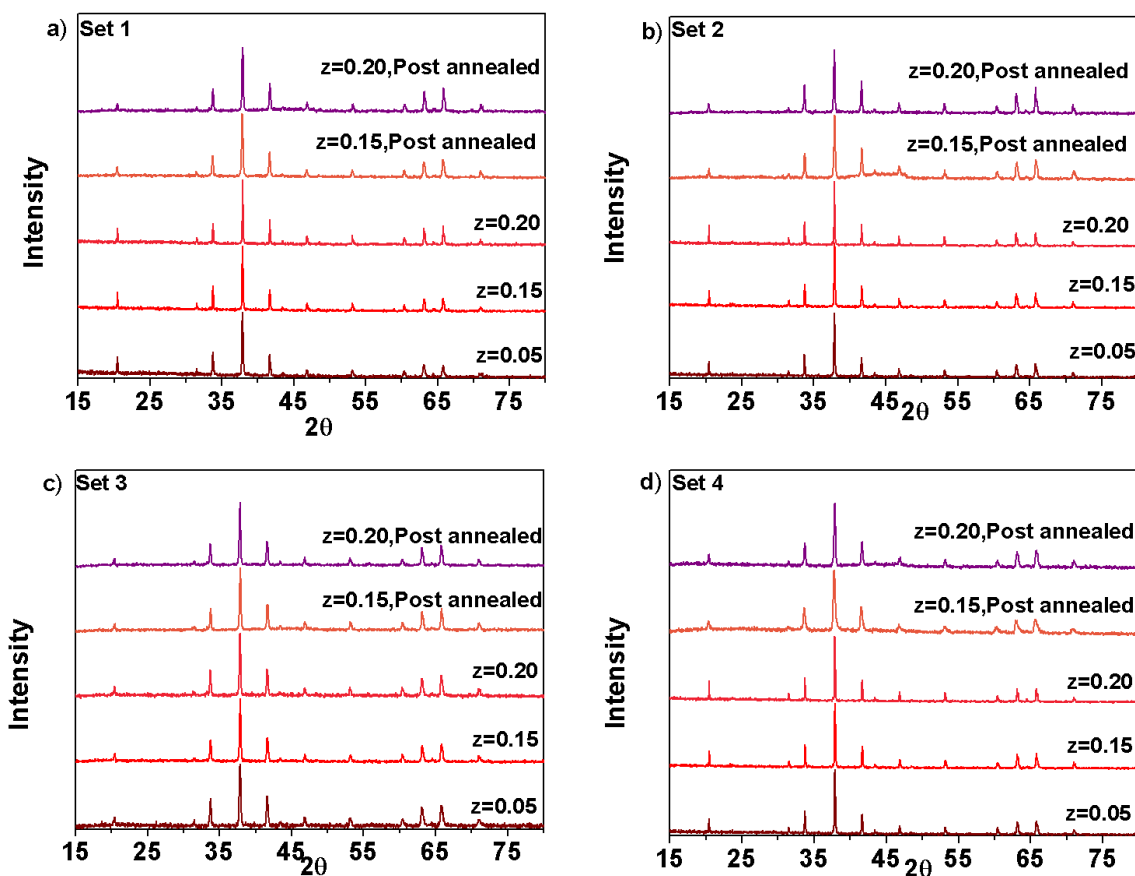


**Figure 3-1:** Powder XRD patterns collected from  $Y_{3-z}Ce_zAlFe_4O_{12}$ . Figure 3-1 (a) represents set 1, (b) represents set 2, (c) represents set 3, and (d) represents set 4. (Set descriptions are given in table 3-1)

### 3.3.2 Ce $L_3$ -edge XANES spectra:

Ce  $L_3$ -edge XANES spectra were collected from all samples to understand how the Ce oxidation state changed depending on concentration and synthesis conditions, and are presented in Figure 3. The spectra show two distinct features resulting from  $2p \rightarrow 4f/5d$  excitations.<sup>72,102,132,133</sup> Large changes in the lineshape, absorption-energy, and spectral intensity are observed in these spectra depending on the Ce oxidation state (4+ vs. 3+).<sup>72,132–134</sup> An increase in the oxidation state will result in fewer electrons being available to screen the nuclear charge and, therefore, more

energy is required to excite core electrons leading to an increase in the observed absorption energy of XANES spectra.<sup>133–136</sup> Four features are reported in spectra from Ce<sup>4+</sup> containing materials because of a pre-edge, quadrupolar 2p → 4f transition, and three dipolar, 2p → 5d transitions resulting from changes in the Ce 4f final-state occupancies (4f<sup>2</sup>, 4f<sup>1</sup>, and 4f<sup>0</sup>).<sup>132–134,137–139</sup> The excitation of a 2p electron from Ce<sup>3+</sup> only results in one intense peak being observed in the Ce L<sub>3</sub>-edge XANES spectra.<sup>140</sup> Examination of the spectra in Figure 3-2 shows two dominant features at different energies, which indicate the presence of trivalent and tetravalent Ce.<sup>72,102</sup> The lower energy peak corresponds primarily to Ce<sup>3+</sup> while the higher energy peak corresponds to Ce<sup>4+</sup>.<sup>72,132,133</sup>

The normalized Ce L<sub>3</sub>-edge spectra (Fig 3-2) show changes in lineshapes when comparing the as-synthesized samples to the post annealed samples. The intense feature located at ~5727 eV indicates the presence of Ce<sup>3+</sup> as the major oxidation state for all samples. The Ce L<sub>3</sub>-edge XANES spectra from sets 1 to 3 show an increase in intensity of the Ce<sup>4+</sup> feature in the post annealed samples. The oxidation of Ce<sup>3+</sup> to Ce<sup>4+</sup> for post annealed samples results from the temperature-dependant Ce<sup>3+</sup>/Ce<sup>4+</sup> redox couple ( $2\text{Ce}^{4+} + \text{O}^{2-} \rightleftharpoons 2\text{Ce}^{3+} + 1/2\text{O}_2$ ).<sup>132,133,137,141</sup> As the temperature decreases, the equilibrium shifts towards Ce<sup>4+</sup>.<sup>132–134</sup> The XRD patterns show no change in the structure of the post annealed samples, demonstrating the structural integrity of the garnet-type structure. The garnet structure can maintain a charge balanced system with the presence of Ce<sup>4+</sup> along with Ce<sup>3+</sup> by either reducing Fe<sup>3+</sup> to Fe<sup>2+</sup> (which has been suggested previously)<sup>27,72</sup> or by incorporating more oxygen into the structure to charge compensate. This is further explored below during the discussion of the Fe K-edge XANES spectra (see Section 3.3.3)

As indicated above, Ce L<sub>3</sub>-edge XANES spectra result (primarily) from the excitation of 2p electrons to 5d states and are very sensitive to variations in oxidation state. It is observed in Fig 3-

2 that the average Ce oxidation state increases with increasing Ce content in the system. The average Ce oxidation state is higher in post-annealed samples and the  $\text{Ce}^{3+}:\text{Ce}^{4+}$  ratio also depends on the amount of Ce incorporation into the system. Normalized Ce L<sub>3</sub>-XANES spectra from  $\text{Y}_{2.85}\text{Ce}_{0.15}\text{AlFe}_4\text{O}_{12}$  are presented in Figure 3-3, Figure 3-4, and Figure 3-5 to understand the effect of starting material, annealing condition, and cooling rate after annealing, respectively. The spectra from  $\text{Y}_{2.80}\text{Ce}_{0.20}\text{AlFe}_4\text{O}_{12}$  shows the same trend in spectral changes the spectra from  $\text{Y}_{2.85}\text{Ce}_{0.15}\text{AlFe}_4\text{O}_{12}$ , and are presented in Appendix A.

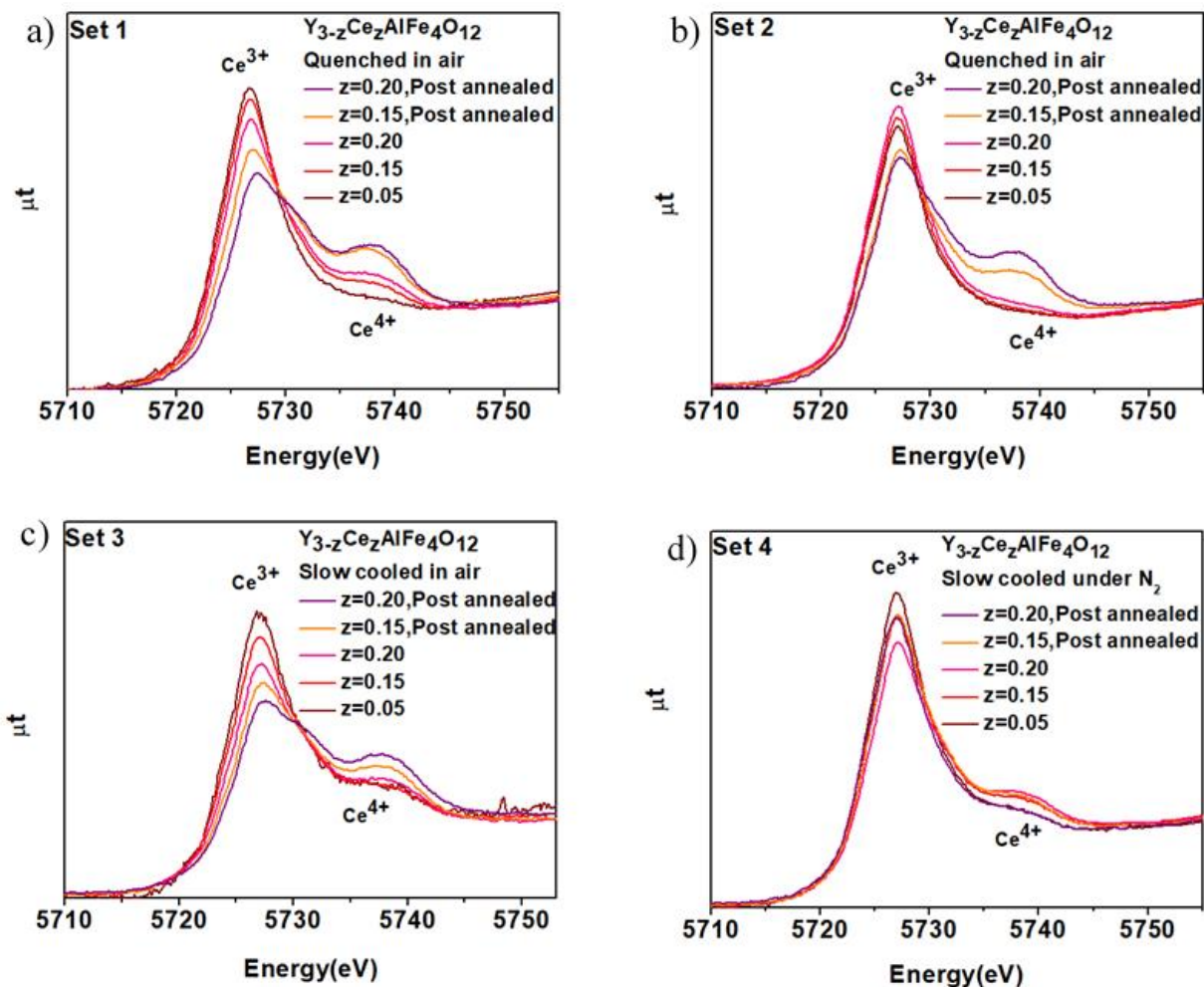


**Figure 3-2:** Normalized Ce L<sub>3</sub> XANES spectra from (a) set 1 ( $Ce^{4+}$  was used as starting material and was quenched in air), (b) set 2 ( $Ce^{3+}$  was used as starting material and was quenched in air), (c) set 3 ( $Ce^{3+}$  was used as starting material and was slow cooled in air), and (d) set 4 ( $Ce^{3+}$  was used as starting material and was slow cooled under  $N_2$ )

Figure 3-3 shows how the spectra change depending on the Ce-containing starting material used to prepare set 1 and set 2 (see Table 3-1). As described earlier, the post-annealed samples showed a greater concentration of  $Ce^{4+}$  (as compared to the as-synthesized materials). Figure 3-3 (a) represents as-synthesized samples (quenched from 1400 °C to room temperature) and Figure

3-3 (b) represents the spectra from the samples post-annealed at 800 °C. The spectra shown in Fig 3-3 demonstrate that the use of a  $\text{Ce}^{4+}$ -containing starting material results in a higher average oxidation state of Ce. The Ce  $L_3$ -edge XANES spectra from  $\text{Y}_{2.80}\text{Ce}_{0.20}\text{AlFe}_4\text{O}_{12}$  show the same phenomenon, and are shown in Figure A-1. The  $\text{Ce}^{3+}:\text{Ce}^{4+}$  ratio in these materials was also observed to vary depending on the oxidation state of the Ce-containing starting material used to synthesize these materials.

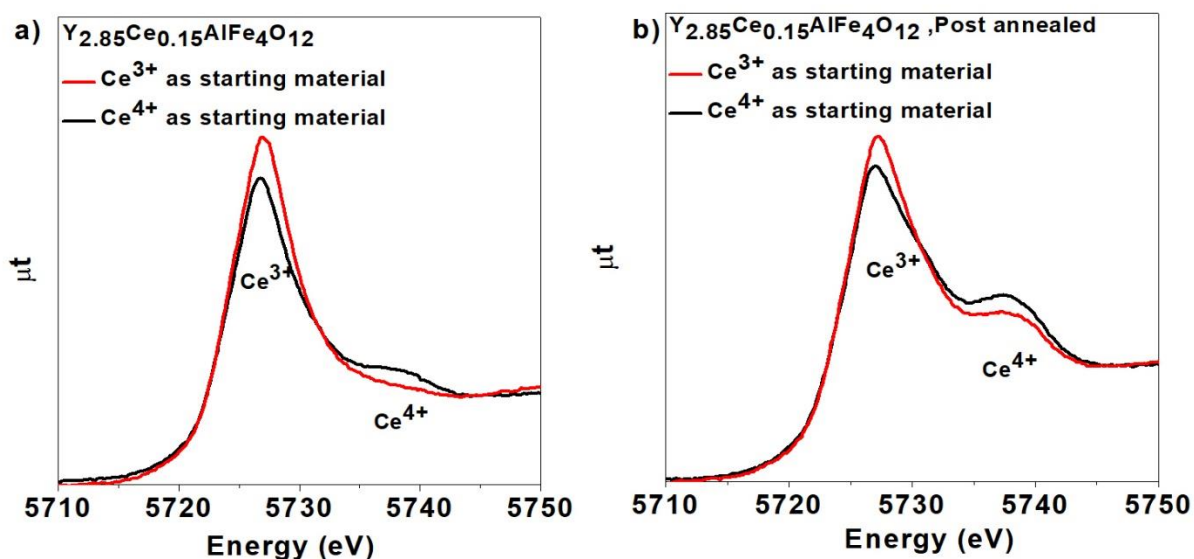


**Figure 3-3:** Normalized Ce  $L_3$ -edge XANES spectra from  $\text{Y}_{2.85}\text{Ce}_{0.15}\text{AlFe}_4\text{O}_{12}$  showing the change in Ce oxidation state that occurs depending on starting material. (a) Represents as-synthesized samples annealed under the same conditions and then quenched in air directly from 1400°C. (b) Represents samples that were post-annealed at 800°C.

Normalized Ce  $L_3$ -edge XANES spectra from  $\text{Y}_{2.85}\text{Ce}_{0.15}\text{AlFe}_4\text{O}_{12}$  are presented in Figure 3-4 to understand the effect of annealing condition on the Ce oxidation state. Annealing under  $\text{N}_2$  gas reduces the amount of oxygen present during high temperature annealing which creates a reducing environment.<sup>137,138</sup> The spectral changes observed in Fig. 3-4 indicates that samples

annealed under air contain a higher  $\text{Ce}^{4+}$  concentration than the samples annealed under  $\text{N}_2(\text{g})$ . It can be concluded that the lack of  $\text{O}_2(\text{g})$  inhibits the temperature-dependent  $\text{Ce}^{3+}/\text{Ce}^{4+}$  redox couple, which results in a lower average Ce oxidation state. However, the spectra presented in Fig 3-2(d) do show that a limited amount of  $\text{Ce}^{4+}$  was observed in the samples annealed under  $\text{N}_2(\text{g})$ , which is likely a result of the purity of the  $\text{N}_2(\text{g})$  used and the presence of O-containing impurities such as  $\text{H}_2\text{O}$ . The observation of a greater concentration of  $\text{Ce}^{4+}$  in the samples annealed in air vs. those annealed in  $\text{N}_2(\text{g})$  demonstrates the importance of the  $\text{O}_2(\text{g})$  partial pressure to the average Ce oxidation state in these materials.

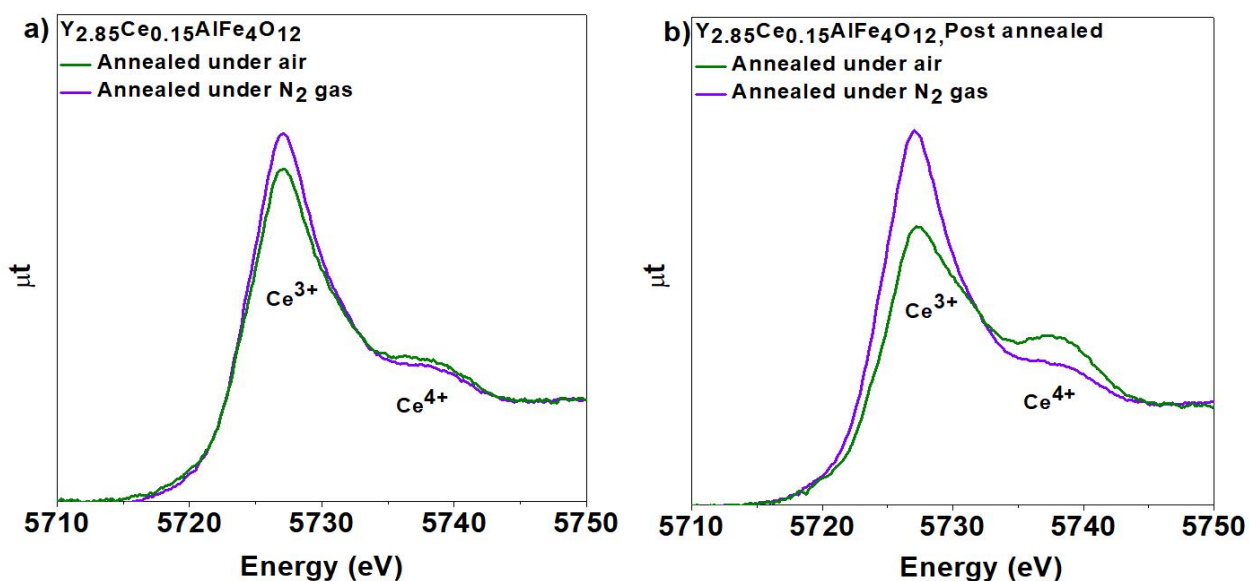


**Figure 3-4:** Normalized Ce L<sub>3</sub>-edge XANES spectra from  $\text{Y}_{2.85}\text{Ce}_{0.15}\text{AlFe}_4\text{O}_{12}$  showing the change in Ce oxidation state that occurs depending on the annealing environment. All materials were synthesized using  $\text{Ce}(\text{NO}_3)_3 \cdot 6\text{H}_2\text{O}$  as the starting material. (a) Compares the spectra from the materials that were synthesized under  $\text{N}_2(\text{g})$  or air followed by slow cooling to room temperature. (b) Compares the spectra from the materials that were synthesized under  $\text{N}_2(\text{g})$  or air and then post-annealed at 800°C.

Normalized Ce L<sub>3</sub>-edge XANES spectra are presented in Figure 3-5 to understand the effect of cooling rate on the Ce oxidation state. Quenching in air after heating at 1400°C (as-



synthesized) results in a lower average Ce oxidation state compared to the material that was slow cooled to room temperature. This observation can be explained by the temperature-dependent equilibrium that exists between  $\text{Ce}^{3+}$  and  $\text{Ce}^{4+}$ , where the oxidation of  $\text{Ce}^{3+}$  to  $\text{Ce}^{4+}$  is an exothermic process.<sup>132,134,141</sup> As the temperature of the system decreases, the equilibrium shifts towards the oxidized state. The higher  $\text{Ce}^{4+}$  concentration observed in the spectra from the slow cooled samples resulted from the exposure of these samples to lower temperatures for longer periods of time.

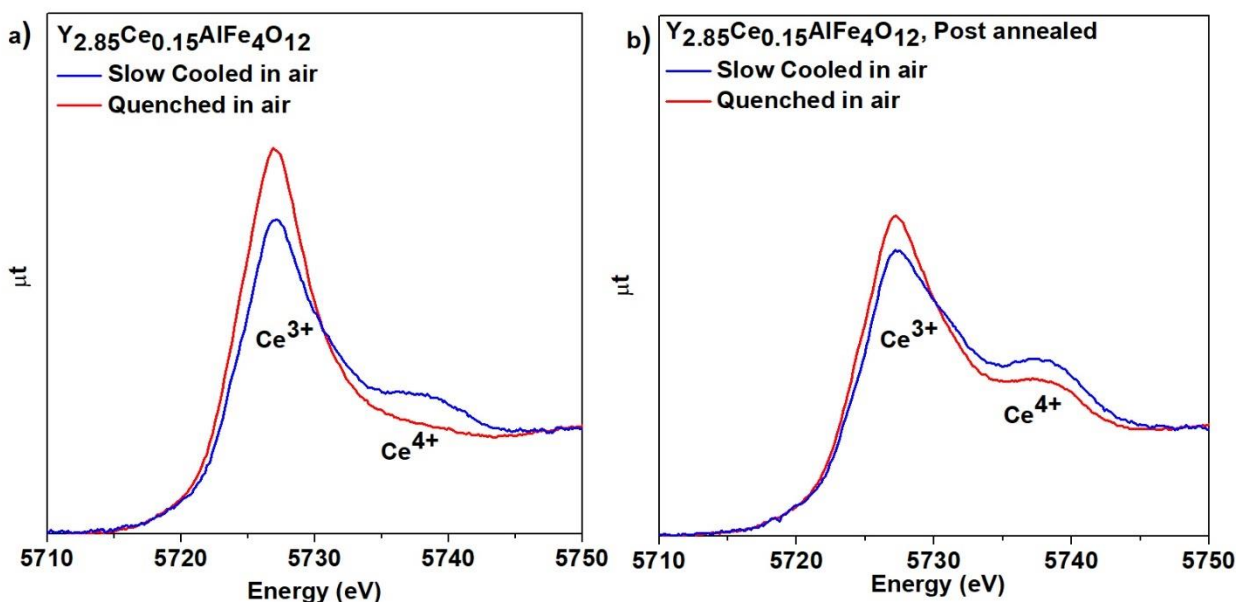


**Figure 3-5:** Normalized Ce L<sub>3</sub>-edge XANES spectra from Y<sub>2.85</sub>Ce<sub>0.15</sub>AlFe<sub>4</sub>O<sub>12</sub> showing the change in Ce oxidation state that occurs depending on the cooling rate used after high temperature annealing. All materials were synthesized using Ce(NO<sub>3</sub>)<sub>3</sub>·6H<sub>2</sub>O as the starting material. (a) Compares the spectra from the materials that were slow cooled to room temperature vs. those that were quenched in air from 1400 °C. (b) Compares the spectra from the materials that were post-annealed at 800°C.

### 3.3.3 Fe K-edge XANES spectra:

It was demonstrated above by examination of the Ce L<sub>3</sub>-edge XANES spectra that the Y<sub>3-z</sub>Ce<sub>z</sub>AlFe<sub>4</sub>O<sub>12</sub> system contains both trivalent and tetravalent Ce and that the average Ce oxidation state increased when the materials were post-annealed at 800 °C (compared to the as-synthesized and quench-cooled materials). This observation could imply that the O stoichiometry was higher in the post-annealed materials or that Fe was (partially) reduced from 3+ to 2+ to charge compensate the system. Fe K-edge XANES spectra are sensitive to the oxidation state and coordination number of Fe.<sup>96,120,142</sup> The normalized Fe K-edge XANES spectra from all sets are presented in Figure 3-6. The spectra can be divided into two regions: the pre-edge region (feature A) and the main edge region (feature B). The pre-edge region (feature A) represents 1s → 3d transitions while the main-edge region (feature B) represents 1s → 4p transitions.<sup>95,125</sup> As described in section 2.5.3, the decrease in intensity of the pre-edge region followed by the increase in intensity of the main-edge indicates an increase of the Fe coordination number (CN).

Fe K-edge XANES spectra collected from Y<sub>3</sub>Fe<sub>5</sub>O<sub>12</sub> show the main-edge feature at ~7127eV and pre-edge feature at ~7112eV, which indicates the presence of Fe<sup>3+</sup> in the system, as would be expected based on the chemical formula. Normalized Fe K-edge XANES spectra from Y<sub>3-z</sub>Ce<sub>z</sub>AlFe<sub>4</sub>O<sub>12</sub> (Figure 3-6) are similar to those found in the spectrum from Y<sub>3</sub>Fe<sub>5</sub>O<sub>12</sub>. This observation confirms that the Fe oxidation state in the Y<sub>3-z</sub>Ce<sub>z</sub>AlFe<sub>4</sub>O<sub>12</sub> is 3+ as a (partial) reduction of Fe<sup>3+</sup> to Fe<sup>2+</sup> would lead to lower energy pre- and main-edge features being observed, which was not the case here.<sup>95,96</sup> Normalized Fe K-edge spectra from set 1, set 2, and set 3 show a decrease in intensity of the pre-edge region followed by an increase in intensity (and slight increase in energy) of the main-edge region from the post annealed samples, which indicates an increase of the Fe coordination number in the post annealed samples compared to the as-synthesized materials.

This change is subtle in the spectra from the set 2 and set 3 samples while the spectra from set 4 show little to no change. The limited change observed in the Fe K-edge spectra from the set 4 samples is understandable considering that these materials were synthesized under a  $N_2(g)$  environment and no significant differences in the Ce  $L_3$ -edge spectra from the as-synthesized vs. post-annealed samples were observed when the composition was held constant (cf., Fig. 3-2(d)).

Examination of the Ce  $L_3$ -edge XANES spectra presented in Fig. 3-2 established the presence of a higher  $Ce^{4+}$  concentration in the post annealed samples compared to the as-synthesized samples when the materials were annealed in air. The increase in Fe CN observed in the post annealed samples along with the presence of more  $Ce^{4+}$  indicates the presence of excess oxygen in the structure to maintain a charge balanced system. It is proposed here that the excess O is incorporated into unoccupied interstitial sites in the garnet structure. It should be emphasized that little to no change in the Ce oxidation state was observed along with little to no change in the CN of Fe when the system was annealed under  $N_2(g)$  (see Figs. 3-2(d), 3-4, and 3-6). This further indicates the importance of the  $O_2(g)$  partial pressure to the oxidation state of Ce observed in these materials and provides more evidence to support the incorporation of excess oxygen in the garnet-type structure to charge balance the (partial) oxidation of  $Ce^{3+}$  to  $Ce^{4+}$ .

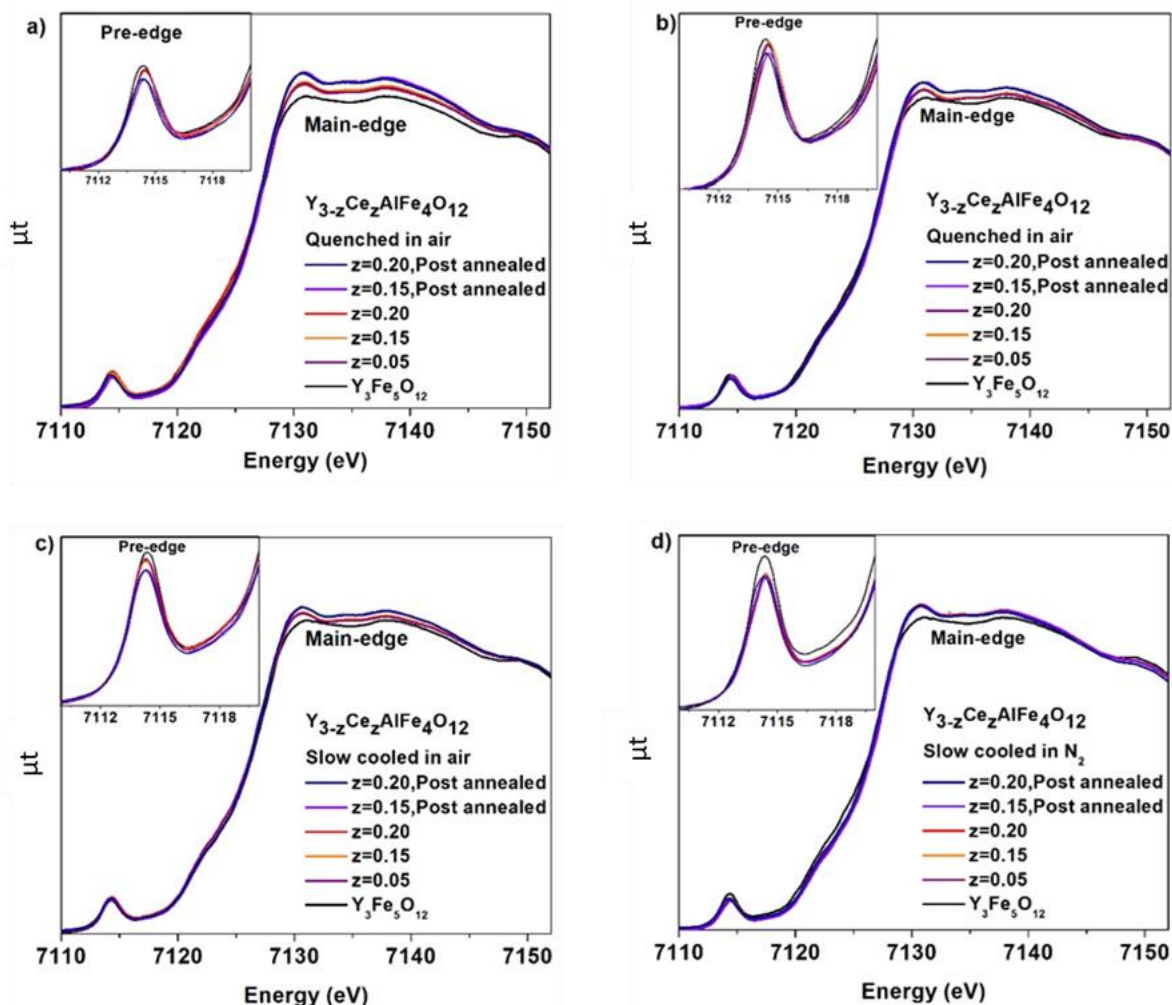


**Figure 3-6:** Normalized Fe K-edge XANES spectra from (a) set 1 ( $Ce^{4+}$  was used as starting material and was quenched in air), (b) set 2 ( $Ce^{3+}$  was used as starting material and was quenched in air), (c) set 3 ( $Ce^{3+}$  was used as starting material and was slow cooled in air), and (d) set 4 ( $Ce^{3+}$  was used as starting material and was slow cooled under  $N_2(g)$ ).

### 3.4 Conclusions:

The study has shown by examination of XANES spectra that  $Y_{3-z}Ce_zAlFe_4O_{12}$  contains both  $Ce^{4+}$  and  $Ce^{3+}$ . Further, it has been shown here that the average oxidation state of Ce in these materials changes depending on starting material, annealing condition, cooling rate, post annealed treatment, and/or concentration of Ce. Analysis of the Fe K-edge XANES spectra have confirmed the presence of  $Fe^{3+}$ . The question then becomes: how do the materials maintain a charge balance system? At lower annealing temperatures, the Ce redox couple shifts towards  $Ce^{4+}$  which leads to incorporation of excess oxygen into the crystal structure to charge balance the system. The increase in average Fe coordination number in the post annealed samples, as determined by analysis of the Fe K-edge XANES spectra, confirms the incorporation of excess oxygen in the garnet-type structure. It is proposed here that  $Y_{3-z}Ce_zAlFe_4O_{12}$  incorporates excess oxygen into unoccupied interstitial sites to maintain a charge balanced system, which requires this oxygen-stuffed garnet system to be represented as  $Y_{3-z}Ce_zAlFe_4O_{12+\delta}$ .

## 4 Conclusions and Future work

### 4.1 Conclusions and significance:

The studies presented in this thesis have contributed to a broader understanding of how to tailor crystalline materials for nuclear waste sequestration applications. The initial study of the thesis (Chapter 2) has shown how various ions can substitute into the A- and B-sites. Further, substitution into the X-site was studied to understand how large actinide elements could be incorporated in garnet-type oxides. The factors that affect the oxidation state have been studied using simulator elements (e.g., Ce; Chapter 3). The conclusions from this thesis are important because two important factors were pointed out: i) corrosion products found in HLW have specific site preferences in the garnet structure that can affect how much of the waste elements can be incorporated in the structure; and ii) the multiple oxidation states of various radioactive nuclides can cause an oxygen stuffed garnet structure.

#### 4.1.1 Effect of substitution on the A- and B-site preference:

The A- and B-site preference in garnet type oxides was investigated in Chapter 2. The change in average coordination number of  $\text{Al}^{3+}$ ,  $\text{Ga}^{3+}$ , and  $\text{Fe}^{3+}$  in quinary and quaternary materials was studied by analysis of XRD patterns and XANES spectra. The site occupancies of  $\text{Al}^{3+}$ ,  $\text{Ga}^{3+}$ , and  $\text{Fe}^{3+}$  in the quinary garnet system are affected by different factors, including: the degree of interactions of the cation valence s- and p-states with the anion, concentration, and cation radius. It was mentioned earlier that the garnet structure can accommodate a wide variety of elements and the contributing factors for metal site preference has been studied in quinary garnet systems. In the quinary system (i.e.,  $\text{Y}_3\text{Al}_x\text{Ga}_y\text{Fe}_{5-x-y}\text{O}_{12}$ ), the A- and B- sites contain three different cations which makes it difficult to study by analysis of diffraction data alone. Analyzing the collected XANES

spectra from the quinary system has established that all three factors (i.e., the degree of interactions of the cation valence s- and p-states with the anion, concentration, and cation radius) contribute to the site occupancies observed in this system.

#### **4.1.2 Effect synthesis conditions on the oxidation state of Ce:**

Only dodecahedral sites and octahedral sites are considered to accommodate actinides due to their large dimensions.<sup>22,27,72,78</sup> The complex oxidation state of some actinides makes it difficult to understand the local structural of garnet. In the third chapter, Ce-substituted garnet-type materials were synthesized to understand the factors that can contribute to changes in the oxidation state how the structure changes to compensate the oxidation state changes. Ce is considered an actinide “simulator” for Pu, in particular, owing to its similar ionic radius, coordination environment, and oxidation states that it can attain.<sup>134</sup> The substitution of U or Pu for Y requires the cations to be trivalent, which is hard to control, since oxidation can occur easily.<sup>72</sup> Since cerium (Ce) can be considered an analogue of actinide elements such as plutonium (Pu), studying the factors that affect the oxidation state of Ce helps to mimic the factors that can affect the actinides. Four different sets of garnet were synthesized and the collected XRD patterns indicated the formation single phase garnet regardless of changes in starting material, annealing condition, cooling rate, post annealed treatment, and/or concentration of Ce. Ce was found to be present in two different oxidation states (3+ and 4+) where the amount of  $\text{Ce}^{4+}$  was a function of concentration of Ce, starting materials, annealing condition, cooling rate, and post annealing. The change in oxidation of Ce gives rise to the difficulty to maintain a charge-balanced system. Fe K-edge XANES spectra collected from four different sets of  $\text{Y}_{3-z}\text{Ce}_z\text{AlFe}_4\text{O}_{12}$  materials revealed two interesting facts. According to the XANES spectra, the oxidation state of Fe is 3+ and the average CN of Fe increases for the post annealed samples except for the samples annealed under nitrogen

gas. Increase in average coordination number of Fe for post annealed samples suggests the incorporation of excess oxygen into unoccupied interstitial sites.

#### **4.2 Direction for future work:**

A greater understanding of the effect of chemical substitution on the local structure of garnet has been achieved in this thesis using X-ray diffraction and XANES. The studies in this thesis have shown that garnet can accommodate rare earth elements (Y and Ce) and corrosion products ( $\text{Al}^{3+}$  and  $\text{Fe}^{3+}$ ), and that it is also possible for the garnet structure to incorporate excess oxygen when required to charge balance the system. The resistance to radiation damage is also a vital factor that needs to be considered to determine ideal crystalline wasteforms. Thus, one avenue for future studies could be to investigate the effect of radiation induced structural damage on the structure of synthetic garnet. Depending on composition, the radiation resistance can vary for different garnet type structures.<sup>28,75,76,143</sup> Crystalline garnet materials could be implanted with high energy heavy ions to mimic radiation induced structural damage.

Garnet type oxides have been synthesized with various synthetic methods.<sup>144–151</sup> It has been shown experimentally that other synthetic methods (i.e, sol-gel, co-precipitation) can result in the annealing temperature required to prepare crystalline materials being lowered, which can be cost and energy efficient for industrial purpose. An investigation of the effect of synthesis method and/or annealing temperature on the resistance to radiation-induced structural damage of garnet-type oxides can be done.

Inclusion of radioactive nuclides into crystalline ceramic provokes a gradual change as the impact of radioactive decay can lead to a failed container situation in a geological repository. As a result, the wasteform could be exposed to groundwater. Another scope for future study could be the investigation of the chemical durability of garnet type oxides by conducting leaching



experiments using different temperatures and media (i.e, acid or basic media). The use of acidic and basic solutions also speeds up the leaching of the materials and would effectively simulate the long-term exposure of the wasteform to groundwater.<sup>152–155</sup> Therefore, it is important to study the corrosion behaviour of garnet type oxide using neutral ground water, acidic or basic environment, and conducting different temperature dependent leaching study.

## References:

1. Asif, M. & Muneer, T. Energy supply, its demand and security issues for developed and emerging economies. *Renew. Sustain. Energy Rev.* **11**, 1388–1413 (2007).
2. *Nuclear Energy Outlook*. (Nuclear Energy Agency, The Organisation for Economic Co-operation and Development, 2008).
3. United Nations, Department of Economic and Social Affairs. *World Population Prospects: The 2015 Revision, Key Findings and Advance Tables*. (2015).
4. Höök, M. & Tang, X. Depletion of fossil fuels and anthropogenic climate change—A review. *Energy Policy* **52**, 797–809 (2013).
5. Ewing, R. C. The Nuclear Fuel Cycle versus The Carbon Cycle. *Can. Mineral.* **43**, 2099–2116 (2005).
6. Sims, R. E. H., Rogner, H.-H. & Gregory, K. Carbon emission and mitigation cost comparisons between fossil fuel, nuclear and renewable energy resources for electricity generation. *Energy Policy* **31**, 1315–1326 (2003).
7. Lund, H. Renewable energy strategies for sustainable development. *Energy* **32**, 912–919 (2007).
8. Menyah, K. & Wolde-Rufael, Y. CO<sub>2</sub> emissions, nuclear energy, renewable energy and economic growth in the US. *Energy Policy* **38**, 2911–2915 (2010).
9. Jewell, J. Ready for nuclear energy?: An assessment of capacities and motivations for launching new national nuclear power programs. *Energy Policy* **39**, 1041–1055 (2011).
10. *Inventory of Radioactive Waste in Canada*. (2012).
11. Whittle, K. R. *Nuclear Materials Science*. (IOP science, 2013). doi:10.1088/978-0-7503-1104-5
12. Ojovan, M. I. & Lee, W. E. Introduction to Immobilisation. *An Introd. to Nucl. Waste Immobil.* 1–6 (2014). doi:10.1016/B978-0-08-099392-8.00001-2
13. Ojovan, M. I. & Lee, W. E. *An introduction to nuclear waste immobilization*. (2005).
14. Ewing, R. C. Nuclear waste forms for actinides. *Proc. Natl. Acad. Sci. U. S. A.* **96**, 3432–3439 (1999).
15. McCloy, J. S. & Goel, A. Glass-ceramics for nuclear-waste immobilization. *Mater. Res. Soc.* **42**, 233–240 (2017).
16. Caurant, D., Loiseau, P., Bardez, I. & Quintas, A. *Glasses, Glass-Ceramics and Ceramics for Immobilization of Highly Radioactive Nuclear Wastes*. (Nova Science Publishers, Inc., 2009).
17. Donald, I. W., Metcalfe, B. L. & Taylor, R. J. The immobilization of high level radioactive wastes using ceramics and glasses. *J. Mater. Sci.* **32**, 5851–5887 (1997).
18. Yanikomer, N., Asal, S., Hacıyakupoglu, S. & Erenturk, S. A. New Solidification Materials in Nuclear Waste Management. *Int. J. Eng. Technol.* **2**, 76–82 (2016).
19. Ewing, R. C., Whittleston, R. A. & Yardley, B. W. D. Geological disposal of nuclear waste: A primer. *Elements* **12**, 233–237 (2016).

20. Hilemna, B. *Nuclear waste disposal. Environment Science and Technology (ACS)* **16**, (1982).
21. Burakov, B. E. *et al.* Synthesis of Garnet/Perovskite-Based Ceramic for the Immobilization of Pu-Residue Wastes. *MRS Proc.* **556**, 55 (1999).
22. Yudintsev, S. V. *et al.* Accommodation of Uranium into the Garnet Structure. *MRS Proc.* **713**, JJ11.28 (2002).
23. Rák, Z., Ewing, R. C. & Becker, U. Role of iron in the incorporation of uranium in ferric garnet matrices. *Phys. Rev. B* **84**, 155128 (2011).
24. Rak, Z., Ewing, R. C. & Becker, U. First-principles investigation of  $\text{Ca}_3(\text{Ti, Zr, Hf, Sn})_2\text{Fe}_2\text{SiO}_{12}$  garnet structure for incorporation of actinides. *Phys. Rev. B - Condens. Matter Mater. Phys.* **83**, 1–8 (2011).
25. Öztürk, Y. *et al.* Cerium-Doped Yttrium-Iron Garnet Thin Films Prepared on Different Substrates Using the Sol-Gel Process Strukturne in Magnetne Lastnosti S Cerijem. *Mater. Technol.* **47**, 59–63 (2013).
26. Yudintsev, S. V., Osheroova, A. A., Dubinin, A. V., Zotov, A. V. & Stefanovsky, S. V. Corrosion Study of Actinide Waste Forms with Garnet-Type Structure. *MRS Proc.* **824**, CC8.20 (2004).
27. Guo, X. *et al.* Thermodynamics of thorium substitution in yttrium iron garnet: comparison of experimental and theoretical results. *J. Mater. Chem. A* **2**, 16945–16954 (2014).
28. Utsunomiya, S., Yudintsev, S. & Ewing, R. C. Radiation effects in ferrate garnet. *J. Nucl. Mater.* **336**, 251–260 (2005).
29. Zhang, J., Livshits, T. S., Lizin, A. A., Hu, Q. & Ewing, R. C. Irradiation of synthetic garnet by heavy ions and  $\alpha$ -decay of  $^{244}\text{Cm}$ . *J. Nucl. Mater.* **407**, 137–142 (2010).
30. Livshits, T. S. Stability of artificial ferrite garnets with actinides and lanthanoids in water solutions. *Geol. Ore Depos.* **50**, 470–481 (2008).
31. Menzer, G. Die Kristallstruckture von granat. *Zeitschrift für Krist.* **63**, 157–158 (1926).
32. Novak, A. G. & Gibbs, G. V. The crystal chemistry of the silicate garnets. *Am. Miner.* **56**, 791–823 (1971).
33. Geller, S. Crystal chemistry of the garnets. *Zeitschrift für Krist.* **125**, 1–47 (1967).
34. Bruno, J. & Ewing, R. C. Spent Nuclear Fuel. *Elements* **2**, 343–349 (2006).
35. Ewing, R. C. Nuclear Fuel Cycle: Environmental Impact. *MRS Bull.* **33**, 338–340 (2008).
36. Hoffert, M. I. *et al.* Advanced technology paths to global climate stability: energy for a greenhouse planet. *Science* **298**, 981–7 (2002).
37. Lenzen, M. Current state of development of electricity-generating technologies: A literature review. *Energies* **3**, 462–591 (2010).
38. Lenzen, M. Life cycle energy and greenhouse gas emissions of nuclear energy: A review. *Energy Convers. Manag.* **49**, 2178–2199 (2008).
39. Abu-Khader, M. M. Recent advances in nuclear power: A review. *Prog. Nucl. Energy* **51**, 225–235 (2009).
40. Hirschberg, G. *et al.* Accumulation of radioactive corrosion products on steel surfaces of VVER

- type nuclear reactors. I. 110mAg. *J. Nucl. Mater.* **265**, 273–284 (1999).
41. Volckaert, G. *et al.* National Inventories and Management Strategies for Spent Nuclear Fuel and Radioactive Waste. Methodology for Common Presentation of Data. (2016).
  42. Nuclear Energy Agency. *Radioactive Waste in Perspective*. (The Organisation for Economic Co-operation and Development, 2010). doi:10.1787/9789264092624-en
  43. Weber, W. J., Navrotsky, A., Stefanovsky, S., Vance, E. R. & Vernaz, E. Materials Science of High-Level Immobilization. *MRS Bulletin* **34**, 46–52 (2009).
  44. Ringwood, a. E., Kesson, S. E., Ware, N. G., Hibberson, W. & Major, a. Immobilisation of high level nuclear reactor wastes in SYNROC. *Nature* **278**, 219–223 (1979).
  45. Ramana, M. V. Shifting strategies and precarious progress: Nuclear waste management in Canada. *Energy Policy* **61**, 196–206 (2013).
  46. Hench, L. L., Clark, D. E. & Campbell, J. High level waste immobilization forms. *Nucl. Chem. Waste Manag.* **5**, 149–173 (1984).
  47. Gin, S. *et al.* An international initiative on long-term behavior of high-level nuclear waste glass. *Mater. Today* **16**, 243–248 (2013).
  48. U.S. Nuclear Regulatory Commission. Radioactive Waste: Production, Storage, Disposal; NUREG/BR-0216, Rev. 2. 1–30 (2002).
  49. Ringwood, A. E. *et al.* Immobilization of high-level nuclear reactor wastes in SYNROC: A current appraisal. *Nucl. Chem. Waste Manag.* **2**, 287–305 (1981).
  50. Lee, W. E., Ojovan, M. I., Stennett, M. C. & Hyatt, N. C. Immobilisation of radioactive waste in glasses, glass composite materials and ceramics. *Adv. Appl. Ceram.* **105**, 3–12 (2006).
  51. Ojovan, M. I. & Lee, W. E. Glassy wasteforms for nuclear waste immobilization. *Metall. Mater. Trans. A Phys. Metall. Mater. Sci.* **42**, 837–851 (2011).
  52. Ojovan, M. I. & Lee, W. E. Immobilisation of Radioactive Wastes in Cement. *An Introd. to Nucl. Waste Immobil.* 205–232 (2005). doi:10.1016/B978-0-08-099392-8.00015-2
  53. Weber, W. J. *et al.* waste and plutonium disposition. (1997).
  54. Nagasaki, S. & Nakayama, S. *Radioactive Waste Engineering and Management*. (2015). doi:10.1007/978-4-431-55417-2
  55. Lumpkin, G. R. Alpha-decay damage and aqueous durability of actinide host phases in natural systems. *J. Nucl. Mater.* **289**, 136–166 (2001).
  56. Yim, M.-S. & Murty, K. L. Materials Issues in Nuclear-waste management. *Jom* **52**, 26–29 (2000).
  57. Weber, W. J. *et al.* Radiation Effects In Crystalline Ceramics For The Immobilization Of High-level Nuclear Waste And Plutonium. *J. Mater. Res.* **13**, 1434–1484 (1998).
  58. Marra, J. C. & Kim, D.-S. Towards Increased Waste Loading in High Level Waste Glasses: Developing a Better Understanding of Crystallization Behavior. *Procedia Mater. Sci.* **7**, 87–92 (2014).
  59. Ewing, R. C. Plutonium and ‘minor’ actinides: Safe sequestration. *Earth Planet. Sci. Lett.* **229**, 165–181 (2005).

60. Ewing, R. C., Weber, W. J. & Clinard, F. W. Radiation Effect in Nuclear Waste Forms For High-Level Radioactive Waste. *Prog. Nucl. Energy* **29**, 63–121 (1995).
61. Ewing, R. C. & Weber, W. J. Actinide Waste Forms and Radiation Effects. *Chem. Actin. Trans. Elem.* **3813**, 3813–3887 (2011).
62. Stefanovsky, S. V., Yudinsev, S. V., Gieré, R. & Lumpkin, G. R. Nuclear waste forms. *Geol. Soc. London, Spec. Publ.* **236**, 37–63 (2004).
63. Raj, K. & Kaushik, C. P. Glass matrices for vitrification of radioactive waste – an Update on R & D Efforts. *IOP Conf. Ser. Mater. Sci. Eng.* **2**, 012002 (2009).
64. Boccaccini, A. R., Bernardo, E., Blain, L. & Boccaccini, D. N. Borosilicate and lead silicate glass matrix composites containing pyrochlore phases for nuclear waste encapsulation. *J. Nucl. Mater.* **327**, 148–158 (2004).
65. Caurant, D. & Gourier, D. *Studies on Ceramics and Glass-Ceramics for Immobilization of High-Level Nuclear Wastes*. (2007).
66. Chen, I. Nuclear Waste Glasses. *Large.Stanford.Edu* 357–364 (2006). doi:10.2113/gselements.2.6.357
67. Ojovan, M. I. & Lee, W. E. Immobilisation of Radioactive Wastes in Glass. *An Introd. to Nucl. Waste Immobil.* 213–249 (2005). doi:10.1016/B978-008044462-8/50019-3
68. Muller, I. & Weber, W. J. Plutonium in Crystalline Ceramics. *MRS Bull.* **26**, 698–706 (2001).
69. Galuskina, I. O. *et al.* Toturite  $\text{Ca}_3\text{Sn}_2\text{Fe}_2\text{SiO}_{12}$ —A new mineral species of the garnet group. *Am. Mineral.* **95**, 1305–1311 (2010).
70. Rák, Z., Ewing, R. C. & Becker, U. Ferric garnet matrices for immobilization of actinides. *J. Nucl. Mater.* **436**, 1–7 (2013).
71. Galuskina, I. O. *et al.* Elbrusite-(Zr)—A new uranian garnet from the Upper Chegem caldera, Kabardino-Balkaria, Northern Caucasus, Russia. *Am. Mineral.* **95**, 1172–1181 (2010).
72. Guo, X. *et al.* Cerium substitution in yttrium iron garnet: Valence state, structure, and energetics. *Chem. Mater.* **26**, 1133–1143 (2014).
73. Laverov, N. P. *et al.* Effect of radiation on properties of confinement matrices for immobilization of actinide-bearing wastes. *Geol. Ore Depos.* **45**, 423–451 (2003).
74. Rák, Z., Ewing, R. C. & Becker, U. Electronic structure and thermodynamic stability of uranium-doped yttrium iron garnet. *J. Phys. Condens. Matter* **25**, 495502 (2013).
75. Utsunomiya, S., Wang, L.-M., Yudinsev, S. & Ewing, R. C. Ion Irradiation Effects in Synthetic Garnets Incorporating Actinides. *MRS Proc.* **713**, JJ11.31 (2011).
76. Yudinsev, S. V. *et al.* Ion-beam irradiation and  $^{244}\text{Cm}$ -doping investigations of the radiation response of actinide-bearing crystalline waste forms. *J. Mater. Res.* **7**, 1–13 (2015).
77. Approaches, N. New Immobilising Hosts and Technologies. *An Introd. to Nucl. Waste Immobil.* (2005).
78. Rák, Z., Ewing, R. C. & Becker, U. Role of iron in the incorporation of uranium in ferric garnet matrices. *Phys. Rev. B - Condens. Matter Mater. Phys.* **84**, 1–10 (2011).
79. Cullity, B. D. *Elements of X-ray diffraction*. (Addison-Wesley Publishing Company INC., 1978).

80. Scott, R. a. X-ray Absorption Spectroscopy. *Compr. Coord. Chem. II* 159–186 (2011). doi:10.1002/9781119951438.eibd0831
81. Newville, M. Fundamentals of XAFS. *Rev. Mineral. Geochemistry* **78**, 33–74 (2014).
82. Regier, T. *et al.* Performance and capabilities of the Canadian Dragon: The SGM beamline at the Canadian Light Source. *Nucl. Instruments Methods Phys. Res. Sect. A Accel. Spectrometers, Detect. Assoc. Equip.* **582**, 93–95 (2007).
83. Hu, Y. F., Zuin, L., Reininger, R. & Sham, T. K. VLS-PGM Beamline at the Canadian Light Source. in *AIP Conference Proceedings* **879**, 535–538 (AIP, 2007).
84. de Groot, F., Vankó, G. & Glatzel, P. The 1s x-ray absorption pre-edge structures in transition metal oxides. *J. Phys. Condens. Matter* **21**, 104207 (2009).
85. Mobilio, S. & Balerna, A. Introduction to the main properties of Synchrotron Radiation. ... -*Italian Phys. Soc.* **82**, 1–24 (2003).
86. Paterson, D. J., Boldeman, J. W., Cohen, D. D. & Ryan, C. G. Microspectroscopy Beamline at the Australian Synchrotron. *AIP Conf. Proc.* **879**, 864–867 (2007).
87. Sham, T. K. & Rivers, M. L. A brief overview of synchrotron radiation. *Rev. Mineral. Geochemistry* **49**, 117–147 (2002).
88. Brown, G. E. & Sturchio, N. C. An Overview of Synchrotron Radiation Applications to Low Temperature Geochemistry and Environmental Science. *Rev. Mineral. Geochemistry* **49**, 1–115 (2002).
89. Maginn, S. J. Analytical Applications of synchrotron radiation. *Analyst* **123**, 19R–29R (1998).
90. Bunker, G. *Introduction to XAFS: A Practical Guide to X-ray Absorption Fine Structure Spectroscopy*. (Cambridge University Press, 2010). doi:10.1017/CBO9781107415324.004
91. Penner-Hahn, J. E. X-ray absorption spectroscopy. *Compr. Coord. Chem. II* 159–186 (2004). doi:10.1038/277089a0
92. de Groot, F. M. F. Novel techniques and approaches to unravel the nature of X-ray absorption spectra. *AIP Conf. Proc.* **882**, 37–43 (2007).
93. de Groot, F. High-resolution X-ray emission and X-ray absorption spectroscopy. *Chem. Rev.* **101**, 1779–1808 (2001).
94. de Groot, F. M. F. X-ray absorption and dichroism of transition metals and their compounds. *J. Electron Spectros. Relat. Phenomena* **67**, 529–622 (1994).
95. Westre, T. E. *et al.* A multiplet analysis of Fe K-edge 1s → 3d pre-Edge features of iron complexes. *J. Am. Chem. Soc.* **119**, 6297–6314 (1997).
96. Sigrist, J. A., Gaultois, M. W. & Grosvenor, A. P. Investigation of the Fe K-edge XANES Spectra from Fe<sub>1-x</sub>Ga<sub>x</sub>SbO<sub>4</sub>: Local versus Nonlocal Excitations. *J. Phys. Chem. A* **115**, 1908–1912 (2011).
97. Yamamoto, T. Assignment of pre-edge peaks in K-edge x-ray absorption spectra of 3d transition metal compounds: electric dipole or quadrupole. *X-Ray Spectrom.* **37**, 572–584 (2008).
98. Weigel, C., Calas, G., Cormier, L., Galois, L. & Henderson, G. S. High-resolution Al L 2,3 -edge x-ray absorption near edge structure spectra of Al-containing crystals and glasses: coordination

- number and bonding information from edge components. *J. Phys. Condens. Matter* **20**, 135219 (2008).
99. Ikeno, H., de Groot, F. M. F., Stavitski, E. & Tanaka, I. Multiplet calculations of L(2,3) x-ray absorption near-edge structures for 3d transition-metal compounds. *J. Phys. Condens. Matter* **21**, 104208 (2009).
  100. Groot, F. De. Multiplet effects in X-ray spectroscopy. *Coord. Chem. Rev.* **249**, 31–63 (2005).
  101. Heald, S. M. *et al.* XAFS and micro-XAFS at the PNC-CAT beamlines. *J. Synchrotron Rad* **6**, 347–349 (1999).
  102. Guo, X. *et al.* Charge-Coupled Substituted Garnets ( $\text{Y}_{3-x}\text{Ca}_{0.5x}\text{M}_{0.5x}\text{Fe}_5\text{O}_{12}$ ) (M = Ce, Th): Structure and Stability as Crystalline Nuclear Waste Forms. *Inorg. Chem.* **54**, 4156–4166 (2015).
  103. Marezio, M., Remeika, J. P. & Dernier, P. D. Cation Distri in  $\text{YAl}_3\text{Ga}_5\text{O}_{12}$  Garnet. *Acta Crystallogr.* **B24**, (1968).
  104. Fischer, P., Halg, W., Stoll, E. & Segmuller, A. X-ray and Neutron Diffraction Study of the Substitutional Disorder in the Yttrium-Iron-Gallium Garnets. *Acta Crystallogr.* **21**, (1966).
  105. Fischer, P., Halg, W., Roggwiler, P., Czerlinsky, E. R. & Bertaut, E. F. Cation Distribution of Y-Fe-Al Garnets. *Solid State Commun.* **16**, 987–992 (1975).
  106. Waychunas, G. A., Apter, M. J. & Brown, G. E. X-ray K-edge absorption spectra of Fe minerals and model compounds: Near-edge structure. *Phys. Chem. Miner.* **10**, 1–9 (1983).
  107. Goodenough, J. B. & Loeb, A. L. Theory of Ionic Ordering, Crystal Distortion, and Magnetic Exchange Due to Covalent Forces in Spinels. *Phys. Rev.* **98**, 391–408 (1955).
  108. Holland, T. J. B. & Redfern, S. A. T. Unit cell refinement from powder diffraction data: the use of regression diagnostics. *Mineral. Mag.* **61**, 65–77 (1997).
  109. Degen, T., Sadki, M., Bron, E., König, U. & Nénert, G. The HighScore suite. *Powder Diffr.* **29**, S13–S18 (2014).
  110. Ravel, B. & Newville, M. ATHENA and ARTEMIS Interactive Graphical Data Analysis using IFEFFIT. *Phys. Scr.* **2005**, 1007 (2005).
  111. Shannon, R. D. Revised effective ionic radii and systematic studies of interatomic distances in halides and chalcogenides. *Acta Crystallogr. Sect. A* **32**, 751–767 (1976).
  112. Denton, A. R. & Ashcroft, N. W. Vegard's law. *Phys. Rev. A* **43**, 3161–3164 (1991).
  113. Krehula, S. *et al.* Synthesis and microstructural properties of mixed iron–gallium oxides. *J. Alloys Compd.* **634**, 130–141 (2015).
  114. Walker, J. D. S. & Grosvenor, A. P. An X-ray absorption spectroscopic study of the metal site preference in  $\text{Al}_{1-x}\text{Ga}_x\text{FeO}_3$ . *J. Solid State Chem.* **197**, 147–153 (2013).
  115. Weigel, C., Calas, G., Cormier, L., Galois, L. & Henderson, G. S. High-resolution Al L<sub>2,3</sub>-edge x-ray absorption near edge structure spectra of Al-containing crystals and glasses: coordination number and bonding information from edge components. *J. Phys. Condens. Matter* **20**, 135219 (2008).
  116. Kim, W., We, J. H., Kim, S. J. & Kim, C. S. Effects of cation distribution for  $\text{AFeO}_3$  (A= Ga, Al). *J. Appl. Phys.* **101**, 09M515 (2007).

117. Grosvenor, A. P. *et al.* Effects of bond character on the electronic structure of brownmillerite-phase oxides,  $\text{Ca}_2\text{B}'_x\text{Fe}_{2-x}\text{O}_5$  ( $\text{B}'=\text{Al, Ga}$ ): an X-ray absorption and electron energy loss spectroscopic study. *J. Mater. Chem.* **19**, 9213 (2009).
118. Dunitz, J. D. & Orgel, L. E. Electronic Properties of Oxides-II Transition-Metal Cation Distribution Amongst Octahedral and Tetrahedral Sites. *J. Phys. Chem. Solids* **3**, 318–323 (1957).
119. Gaultois, M. W., Greedan, J. E. & Grosvenor, A. P. Investigation of coordination changes in substituted transition-metal oxides by K-edge XANES: Beyond the pre-edge. *J. Electron Spectros. Relat. Phenomena* **184**, 192–195 (2011).
120. Walker, J. D. S. & Grosvenor, A. P. An X-ray absorption spectroscopic study of the metal site preference in  $\text{Al}_{1-x}\text{Ga}_x\text{FeO}_3$ . *J. Solid State Chem.* **197**, 147–153 (2013).
121. Grosvenor, A. P. & Greedan, J. E. Analysis of Metal Site Preference and Electronic Structure of Brownmillerite-Phase Oxides ( $\text{A}_2\text{B}'_x\text{B}_{2-x}\text{O}_5$ ;  $\text{A}=\text{Ca, Sr}$ ;  $\text{B}'/\text{B}=\text{Al, Mn, Fe, Co}$ ) by X-ray Absorption. *J. Phys. Chem. C* **113**, 11366–11372 (2009).
122. Nishi, K. *et al.* Deconvolution Analysis of Ga K-Edge XANES for Quantification of Gallium Coordinations in Oxide Environments. *J. Phys. Chem. B* **102**, 10190–10195 (1998).
123. Walker, J. D. S., Hayes, J. R. & Grosvenor, A. P. Examination of the site preference of metals in  $\text{NiAl}_{2-x}\text{Ga}_x\text{O}_4$  spinel-type oxides by X-ray absorption near-edge spectroscopy. *J. Electron Spectros. Relat. Phenomena* **195**, 139–144 (2014).
124. Roschmann, P. Site preference of iron, gallium and aluminum in quasibinary mixed garnets. *J. Phys. Chem Solids* **41**, 569–581 (1980).
125. Wilke, M., Farges, F., Petit, P. E., Brown, G. E. & Martin, F. Oxidation state and coordination of Fe in minerals: An Fe K-XANES spectroscopic study. *Am. Mineral.* **86**, 714–730 (2001).
126. Gaultois, M. W. & Grosvenor, A. P. Coordination-induced shifts of absorption and binding energies in the  $\text{SrFe}_{1-x}\text{Zn}_x\text{O}_3$  system. *J. Phys. Chem. C* **114**, 19822–19829 (2010).
127. Gaultois, M. W. & Grosvenor, A. P. XANES and XPS investigations of  $(\text{TiO}_2)_x(\text{SiO}_2)_{1-x}$ : the contribution of final-state relaxation to shifts in absorption and binding energies. *J. Mater. Chem.* **21**, 1829–1836 (2011).
128. Burakov, B. E., Anderson, E. E., Zamoryanskaya, M. V. & Petrova, M. A. Synthesis and Study of  $^{239}\text{Pu}$ -Doped Gadolinium-Aluminum Garnet. *MRS Proc.* **608**, 419 (1999).
129. Zamoryanskaya, M. V. & Burakov, B. E. Cathodoluminescence of Ce, U and Pu in a Garnet Host Phase. in *MRS Proceedings* **608**, 437 (Cambridge University Press, 1999).
130. Laverov, N. P. *et al.* Synthetic minerals with the pyrochlore and garnet structures for immobilization of actinide-containing wastes. *Geochemistry Int.* **48**, 1–14 (2010).
131. Ewing, R. C., Weber, W. J. & Lian, J. Nuclear waste disposal-pyrochlore ( $\text{A}_2\text{B}_2\text{O}_7$ ): Nuclear waste form for the immobilization of plutonium and ‘minor’ actinides. *J. Appl. Phys.* **95**, 5949–5971 (2004).
132. Aluri, E. R., Bachiu, L. M., Grosvenor, A. P., Forbes, S. H. & Greedan, J. E. Assessing the oxidation states and structural stability of the Ce analogue of brannerite. *Surf. Interface Anal.* **49**, 1335–1344 (2017).
133. Paknahad, E. & Grosvenor, A. P. Investigation of  $\text{CeTi}_2\text{O}_6$ - and  $\text{CaZrTi}_2\text{O}_7$ -containing glass-ceramic composite materials. *Can. J. Chem.* 1–43 (2010).



134. Huynh, L. T. *et al.* How temperature influences the stoichiometry of CeTi<sub>2</sub>O<sub>6</sub>. *Solid State Sci.* **14**, 761–767 (2012).
135. Aluri, E. R. & Grosvenor, A. P. A study of the electronic structure and structural stability of Gd<sub>2</sub>Ti<sub>2</sub>O<sub>7</sub> based glass-ceramic composites. *RSC Adv.* **5**, 80939–80949 (2015).
136. Aluri, E. R. & Grosvenor, A. P. An X-ray absorption spectroscopic study of the effect of bond covalency on the electronic structure of Gd<sub>2</sub>Ti<sub>2</sub>–xSn<sub>x</sub>O<sub>7</sub>. *Phys. Chem. Chem. Phys.* **15**, 10477 (2013).
137. Kotani, A., Kvashnina, K. O., Butorin, S. M. & Glatzel, P. A new method of directly determining the core–hole effect in the Ce L<sub>3</sub> XAS of mixed valence Ce compounds—An application of resonant X-ray emission spectroscopy. *J. Electron Spectros. Relat. Phenomena* **184**, 210–215 (2011).
138. Nachimuthu, P., Shih, W.-C., Liu, R.-S., Jang, L.-Y. & Chen, J.-M. The Study of Nanocrystalline Cerium Oxide by X-Ray Absorption Spectroscopy. *J. Solid State Chem.* **149**, 408–413 (2000).
139. Cabaret, D., Joly, Y., Renevier, H. & Natoli, C. R. Pre-edge structure analysis of Ti K-edge polarized X-ray absorption spectra in TiO<sub>2</sub> by full-potential XANES calculations. *J. Synchrotron Radiat.* **6**, 258–260 (1999).
140. Antonov, V. N., Kukusta, D. A. & Yaresko, A. N. X-ray magnetic circular dichroism in CeFe<sub>2</sub> : First-principles calculations. *Phys. Rev. B* **78**, (2008).
141. Lopez, C. *et al.* Solubility of actinide surrogates in nuclear glasses. *J. Nucl. Mater.* **312**, 76–80 (2003).
142. Wilke, M., Farges, F., Petit, P. E., Brown, G. E. & Martin, F. Oxidation state and coordination of Fe in minerals: An FeK- XANES spectroscopic study. *Am. Mineral.* **86**, 714–730 (2001).
143. Livshits, T. S., Lizin, A. A., Zhang, J. M. & Ewing, R. C. Amorphization of rare earth aluminate garnets under ion irradiation and decay of <sup>244</sup>Cm admixture. *Geol. Ore Depos.* **52**, 267–278 (2010).
144. Geiger, C. A., Armbruster, T. & Lager, G. A. Single-crystal X-ray structure study of synthetic pyrope almandine garnets at 100 and 293 K Neutron Scattering in Mineral, Earth and Environmental Sciences View project Nitrogenous Biosignatures and Implications for Astrobiology View project Single-crystal X-ray structure study of synthetic pyrope almandine garnets at 100 and 293 K. *Am. Mineral.* **77**, 512–521 (1992).
145. Zhang, X. *et al.* Novel synthesis of YAG by solvothermal method. *J. Cryst. Growth* **275**, e1913–e1917 (2005).
146. Inoue, M., Otsu, H., Kominami, H. & Inui, T. Synthesis of Yttrium Aluminum Garnet by the Glycothermal Method. *J. Am. Ceram. Soc.* **74**, 1452–1454 (1991).
147. Xu, X. *et al.* Synthesis of Monodispersed Spherical Yttrium Aluminum Garnet (YAG) Powders by a Homogeneous Precipitation Method. *J. Am. Ceram. Soc.* **95**, 3821–3826 (2012).
148. Lu, Q., Dong, W., Wang, H. & Wang, X. A Novel Way to Synthesize Yttrium Aluminum Garnet from Metal-Inorganic Precursors. *J. Am. Ceram. Soc.* **85**, 490–492 (2004).
149. Han, K. R., Koo, H. J. & Lim, C. S. A Simple Way to Synthesize Yttrium Aluminum Garnet by Dissolving Yttria Powder in Alumina Sol. *J. Am. Ceram. Soc.* **82**, 1598–1600 (2004).
150. Wang, H., Gao, L. & Niihara, K. Synthesis of nanoscaled yttrium aluminum garnet powder by the

- co-precipitation method. *Mater. Sci. Eng. A* **288**, 1–4 (2000).
151. Vaqueiro, P. & López-Quintela, M. A. Influence of Complexing Agents and pH on Yttrium–Iron Garnet Synthesized by the Sol–Gel Method. *Chem. Mater.* **9**, 2836–2841 (1997).
  152. Perevalov, S., Stefanovsky, S. V., Yudintsev, S. V., Mokhov, A. V. & Ptashkin, A. G. Leaching of neptunium from garnet- and murataite-based ceramics. *Radiochim. Acta* **94**, 509–514 (2006).
  153. Ma, J. *et al.* Effects of sintering process, pH and temperature on chemical durability of  $\text{Ce}_{0.5}\text{Pr}_{0.5}\text{PO}_4$  ceramics. *J. Nucl. Mater.* **465**, 550–555 (2015).
  154. Zhao, X. *et al.* Chemical durability and leaching mechanism of  $\text{Ce}_{0.5}\text{Eu}_{0.5}\text{PO}_4$  ceramics: Effects of temperature and pH values. *J. Nucl. Mater.* **466**, 187–193 (2015).
  155. Angeli, F., McGlinn, P. & Frugier, P. Chemical durability of hollandite ceramic for conditioning cesium. *J. Nucl. Mater.* **380**, 59–69 (2008).

## Appendix A:

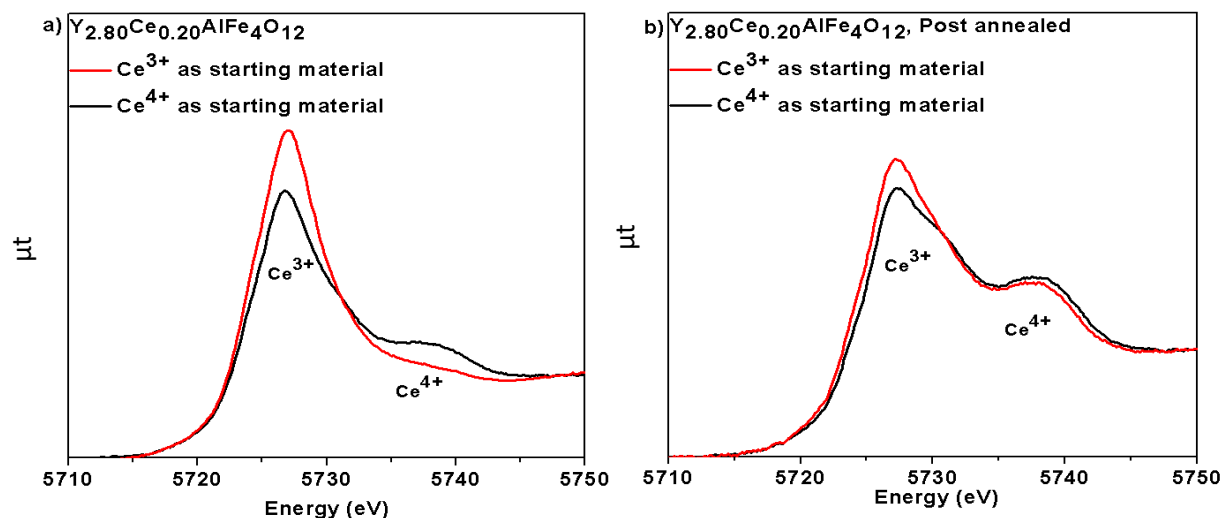


**Figure A-1:** Normalized Ce L<sub>3</sub>-edge XANES spectra from  $\text{Y}_{2.80}\text{Ce}_{0.20}\text{AlFe}_4\text{O}_{12}$  showing the change in Ce oxidation state that occurs depending on the starting material. (a) The Ce L<sub>3</sub>-edge XANES spectra from the as-synthesized samples annealed under the same conditions and then quenched in air from 1400°C. (b) The Ce L<sub>3</sub>-edge XANES spectra from the samples that were post-annealed at 800°C.

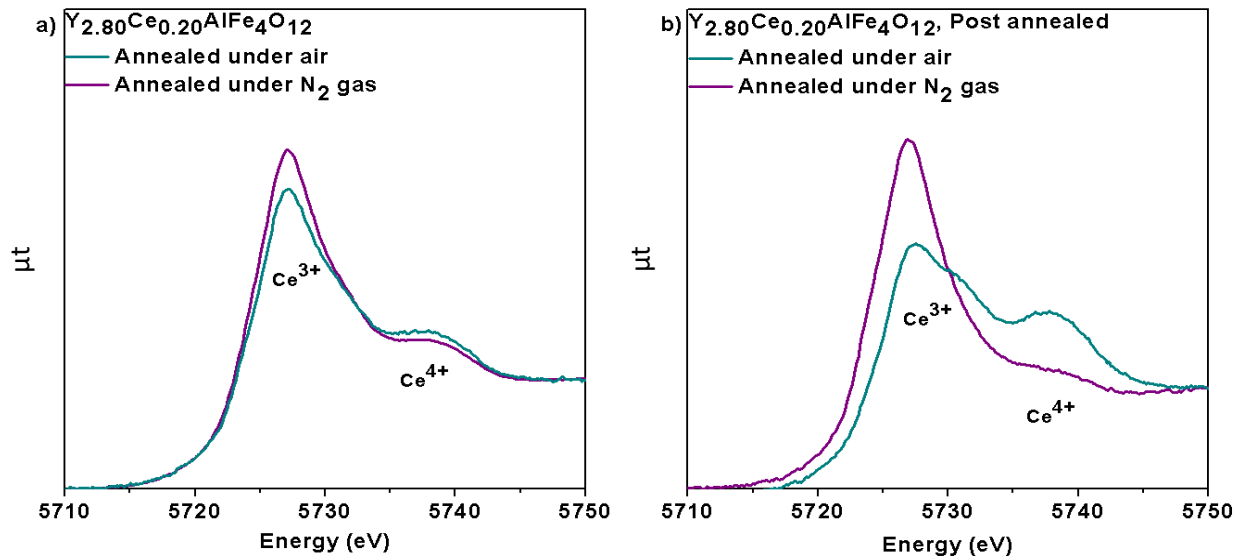


**Figure A-2:** Normalized Ce L<sub>3</sub>-edge XANES spectra from Y<sub>2.80</sub>Ce<sub>0.20</sub>AlFe<sub>4</sub>O<sub>12</sub> showing the change in the Ce oxidation state that occurs depending on annealing environment. (a) The Ce L<sub>3</sub>-edge XANES spectra from the as-synthesized samples formed using the Ce<sup>3+</sup>-containing starting material that slow cooled to room temperature. (b) The Ce L<sub>3</sub>-edge XANES spectra from the samples that were post-annealed at 800°C.

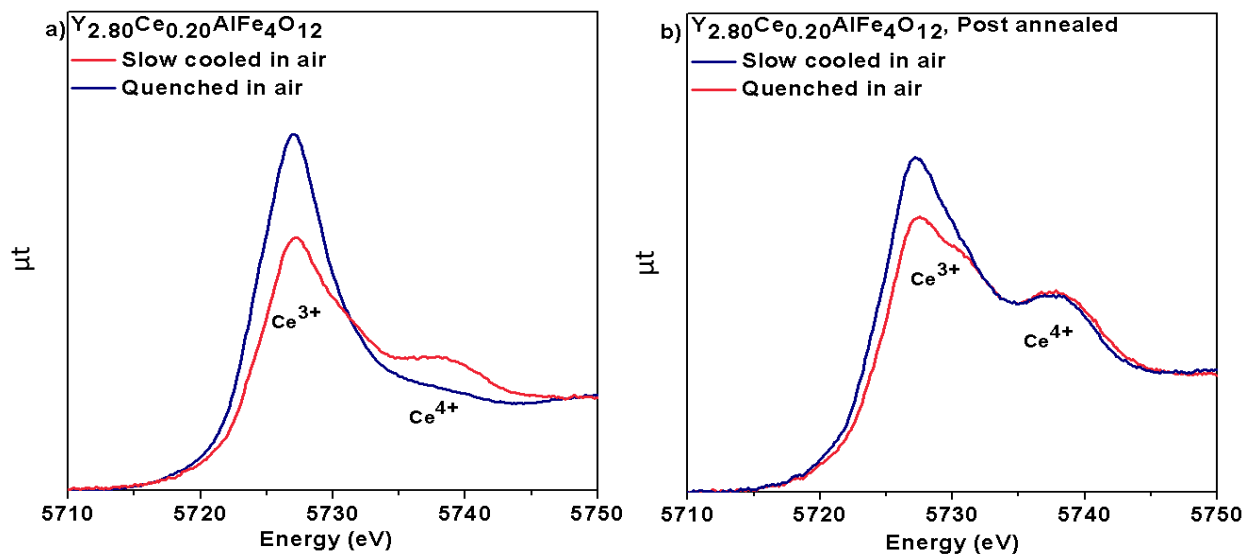


**Figure A-3:** Normalized Ce L<sub>3</sub>-edge XANES spectra from Y<sub>2.80</sub>Ce<sub>0.20</sub>AlFe<sub>4</sub>O<sub>12</sub> showing the change in the Ce oxidation state that occurs depending on the cooling rate used after high temperature annealing. (a) The Ce L<sub>3</sub>-edge XANES spectra from the as-synthesized samples formed using the Ce<sup>3+</sup>-containing starting material and the same annealing conditions. (b) The Ce L<sub>3</sub>-edge XANES spectra from the samples that were post-annealed at 800°C